

Received: 28 July 2010 – Accepted: 13 September 2010 – Published: 21 September 2010

Correspondence to: L. Bugliaro (luca.bugliaro@dlr.de)

Published by Copernicus Publications on behalf of the European Geosciences Union.

Validation of retrievals with simulated data

L. Bugliaro et al.

Title Page

Abstract

Introduction

Conclusions

References

Tables

Figures



Back

Close

Full Screen / Esc

Printer-friendly Version

Interactive Discussion



Abstract

Validation of cloud properties retrieved from passive spaceborne imagers is essential for cloud and climate applications but complicated due to the large differences in scale and observation geometry between the satellite footprint and the independent ground based or airborne observations. Here we illustrate and demonstrate an alternative approach: starting from the output of the COSMO-EU weather model of the German Weather Service realistic three-dimensional cloud structures at a spatial scale of 2.33 km are produced by statistical downscaling and microphysical properties are associated to them. The resulting data sets are used as input to the one-dimensional radiative transfer model libRadtran to simulate radiance observations for all eleven low resolution channels of MET-8/SEVIRI. At this point, both cloud properties and satellite radiances are known such that cloud property retrieval results can be tested and tuned against the objective input “truth”. As an example, we validate a cloud property retrieval of the Institute of Atmospheric Physics of DLR and that of EUMETSAT’s Climate Monitoring Science Application Facility CMSAF. Cloud detection and cloud phase assignment perform well. By both retrievals 88% of the pixels are correctly classified as clear or cloudy. The DLR algorithm assigns the correct thermodynamic phase to 95% of the cloudy pixels and the CMSAF retrieval to 79%. Cloud top temperature is slightly overestimated by the DLR code (+3.1 K mean difference with a standard deviation of 10.6 K) and underestimated by the CMSAF code (−16.4 K with a standard deviation of 37.3 K). Both retrievals account reasonably well for the distribution of optical thickness for both water and ice clouds, with a tendency to underestimation for the DLR and to overestimation for the CMSAF algorithm. Cloud effective radii are most difficult to evaluate and not always the algorithms are able to produce realistic values. The CMSAF cloud water path, which is a combination of the last two quantities, is particularly accurate for ice clouds, while water clouds are overestimated, mainly because of the effective radius overestimation for water clouds.

Validation of retrievals with simulated data

L. Bugliaro et al.

Title Page

Abstract

Introduction

Conclusions

References

Tables

Figures



Back

Close

Full Screen / Esc

Printer-friendly Version

Interactive Discussion



1 Introduction

The determination of cloud macrophysical (e.g. cloud top height), optical (e.g. cloud optical thickness) as well as microphysical (e.g. cloud phase or cloud effective particle radius) is essential for various applications and in general for a deep understanding of cloud and climate processes. For this reason, validation of satellite retrieved cloud properties is crucial and unfortunately complicated. Cloud classification algorithms are usually based on heuristic threshold tests. Independent objective methods to derive cloud properties are often not available, as satellite observations are the only means to observe clouds on a grand scale. Cloud observations from the surface are one possible data source for validation, but we know that systematic differences are to be expected, due to the different observation geometries and scales of the surface and the satellite measurements. For cloud microphysical properties, the situation is even worse: only sparse in-situ data, measured by aircraft, are available. To get any estimates of cloud microphysical properties from the ground, a complex combination of instruments is required to get quantitative results (e.g. microwave radiometry, radar, lidar). In addition, cloud inhomogeneity introduces some bias and considerable noise into the optical thickness and effective radius retrieved at the resolutions of the order 1–5 km (e.g., Zinner and Mayer, 2006). Although one could live with a small bias, noise hampers the validation by in-situ observations, as many data are needed to obtain a statistically significant result.

Thus, we propose and demonstrate an alternative strategy: starting from known cloud fields, the satellite observation has been simulated to produce datasets where radiation as well as cloud properties are fully known, in contrast to the use of satellite observations alone where only the radiation field is available and the accuracy of the derived cloud information cannot be assessed because the “real” cloud properties are not known. On this basis, retrieval algorithms can be tested and tuned, by comparing the retrieved properties with the initial cloud properties. In this paper we simulate a MET-8/SEVIRI scene in Central Europe. To this end, we exploit the output

Validation of retrievals with simulated data

L. Bugliaro et al.

Title Page

Abstract

Introduction

Conclusions

References

Tables

Figures



Back

Close

Full Screen / Esc

Printer-friendly Version

Interactive Discussion



Validation of retrievals with simulated data

L. Bugliaro et al.

Title Page

Abstract

Introduction

Conclusions

References

Tables

Figures

◀

▶

◀

▶

Back

Close

Full Screen / Esc

Printer-friendly Version

Interactive Discussion



of the weather model COSMO-EU to produce realistic three-dimensional cloud fields at a resolution of 7 km. Since this is too coarse for the envisaged satellite instrument we apply a downscaling technique to obtain the necessary input data for the radiative transfer calculations at a more suitable spatial resolution of 2.33 km. The satellite radiances are produced with the one-dimensional radiative transfer solver DISORT 2.0 included in the radiative transfer package libRadtran. The radiative transfer output, i.e. the eleven solar and thermal MET-8/SEVIRI channels, for that particular scene is then used as input to two cloud retrieval algorithms to exemplarily show the potential of the method to objectively test and evaluate the retrieval performance.

The paper is structured as follows: after a short description of the satellite instrument MET-8/SEVIRI selected for this investigation (Sect. 2), the cloud and radiative transfer models (Sect. 3) are presented. Section 4 shows the results of the radiative transfer simulations while Sect. 5 illustrates the retrieval algorithms and Sect. 6 the validation of the retrieval outputs by comparison against the known input cloud properties. Conclusions are found in Sect. 7.

2 MET-8/SEVIRI: a case study

The second generation of the geostationary Meteosat satellites operated by EUMETSAT represents a great advancement compared to the first generation, for the imaging and remote sensing of the Earth's atmosphere and surface and the related physical processes. In particular, the Spinning Enhanced Visible and InfraRed Imager (SEVIRI) aboard Meteosat Second Generation (MSG) combines a fast repeat cycle of 15 min with comprehensive spectral information over the whole Earth disc (see Table 1). SEVIRI comprises 11 spectral channels in the visible and infrared spectral range with a spatial resolution of 3 km×3 km at the sub-satellite point. Furthermore, it is equipped with an additional broadband high resolution visible (HRV) channel with a ground sampling distance of about 1 km at the sub-satellite point. This resolution is comparable to that of the polar orbiting NOAA/AVHRR radiometers (1.1 km at nadir) from which

SEVIRI has inherited some of its spectral channels. This series of satellite instruments has proved to yield data that are excellently suited for meteorological and geophysical applications. Considering also the improved dynamic range of 10 (instead of 8) bits, it is clear that MSG/SEVIRI allows to quantitatively study the life cycle of clouds in a unique way. MSG-1, launched in August 2002 into the geostationary orbit at -3.4° E, is the satellite selected for this case study. The SEVIRI sensor on it has become operational January 2004 under the name of MET-8/SEVIRI.

3 Models

In order to create a synthetic satellite scene two ingredients are needed: 1) a model to produce realistic cloud fields to be used as input for 2) an accurate radiative transfer model to simulate the MET-8/SEVIRI low resolution channels. Both models are presented in the following subsections.

3.1 Cloud model

3.1.1 The COSMO-EU model

For the generation of realistic cloud fields over regions as large as to encompass a considerable variability of cloud as well as surface properties the output of the COSMO-EU model (version 3.15) of the COSMO (*Co*nsortium for *S*mall-scale *Mo*deling) community has been used. The COSMO-EU is a high-resolution non-hydrostatic model (Stappeler et al., 1997) that has been the operational short range weather forecasting tool at the German Weather Service (Deutscher Wetterdienst, DWD) since December 1999. In the operational configuration, with a horizontal mesh size of 7 km on a 325×325 grid, the model domain encompasses all of Central Europe. It has a generalised terrain-following vertical coordinate, which divides the atmosphere into 35 layers from the bottom up to 20 hPa. The prognostic model variables are the wind vector,

Validation of retrievals with simulated data

L. Bugliaro et al.

Title Page

Abstract

Introduction

Conclusions

References

Tables

Figures

◀

▶

◀

▶

Back

Close

Full Screen / Esc

Printer-friendly Version

Interactive Discussion



temperature, pressure perturbation, specific humidity, cloud liquid and ice water, rain and snow water. The model physics includes a level-2 turbulence parameterisation, a delta-2-stream radiation scheme, and a multi-layer soil model. The model contains a grid-scale cloud and precipitation scheme as well as a parameterisation of moist convection (Tiedtke, 1989).

The COSMO-EU vertical profiles used are pressure, temperature, specific humidity, cloud liquid water, cloud ice and snow water together with skin temperature, orography and the land-sea mask. In particular, snow water is associated to ice water because the large autoconversion rates used in the COSMO-EU lead to an under-representation of ice clouds.

As a validation scene for the cloud property retrieval algorithm we selected 12 August 2004, 12:00 UTC, where a frontal system is passing through Central Europe and various cloud types are present.

3.1.2 Downscaling

As the COSMO-EU model, like all weather models, does not provide information on scales below a few kilometres (more precisely 7 km for COSMO-EU), statistical downscaling is applied as a possibility to merge the potential of weather models to provide realistic mesoscale cloud structures in three dimensions and the potential of statistical models to generate realistic small scale variability on the basis of observed statistical characteristics of LWC fields (down to 10 m scale, e.g. Davis, 1996). Venema et al. (2010) use a method similar to the one presented in the following for the downscaling of cloud resolving large eddy simulation model output. A better spatial resolution is mandatory to create input data as realistic as possible in order to assess retrieval performance under real-world conditions.

First, the generalised terrain-following vertical coordinate is transformed to metric coordinates: while temperature and pressure are appropriately interpolated, the other quantities of interest (cloud liquid and ice water, snow water) are mapped such as to preserve the information on the original COSMO-EU vertical resolution and their inte-

Validation of retrievals with simulated data

L. Bugliaro et al.

Title Page

Abstract

Introduction

Conclusions

References

Tables

Figures



Back

Close

Full Screen / Esc

Printer-friendly Version

Interactive Discussion



grated vertical column. At the same time vertical resolution is increased: $\Delta z = 250$ m up to 5000 m a.s.l. and $\Delta z = 550$ m up to 21 500 m a.s.l. All datasets are now given on a regular vertical grid with 50 layers. The horizontal resolution is still unchanged.

Starting from the original horizontal resolution of approximately 7 km corresponding to 325×325 pixels, the resolution of the main output quantities of the COSMO-EU is increased to 2.33 (= 7/3) km. During this procedure the energy density (the Fourier spectrum) of the water fields is forced to obey a 5/3 decay law for small scale variations (“sub-resolution” in the following), as shown by many in-situ measurements (e.g. Davis, 1996; Pinsky and Khain, 2003) while large scale variation and the water content on the original horizontal resolution (7 km) is conserved.

This downscaling algorithm starts with the cloud layer closest to the ground and proceeds, layer by layer, towards cloud top. Variation in the lowest layer are less constrained than in upper layers because a certain vertical correlation of the subgrid variations is imposed following the correlation given on original COSMO-EU resolution. Step by step the 5/3 Fourier power spectrum is forced on the sub-resolution cloud water fields while the total content at the COSMO-EU resolution as given in the COSMO-EU output is conserved. The Fourier spectrum of the original COSMO-EU fields is thus conserved on large scales, while variability at small scales is introduced by continuation of the 5/3 power spectrum below a given wavenumber depending on the size of the COSMO-EU simulation domain.

The phase of the small scale Fourier components of the bottom layer is created randomly while the large scale (COSMO-EU modelled) phases are conserved. Vertical correlation of sub-resolution variations is achieved by retaining part of the small scale phases whenever the algorithm switches to a higher layer.

Figure 1a shows a sub-section of the COSMO-EU input data. Shown is a horizontal cross section through the liquid water content of 350×350 km (at 7 km resolution) at the height layer between 1500 and 1750 m. The related power spectrum is displayed below it. Obviously it shows no clear scaling law behaviour. While at large scales (small wavenumbers) the mesoscale weather structures are not expected to do so, a

Validation of retrievals with simulated data

L. Bugliaro et al.

Title Page

Abstract

Introduction

Conclusions

References

Tables

Figures



Back

Close

Full Screen / Esc

Printer-friendly Version

Interactive Discussion



5/3 power law is expected at ranges between 10–30 km ($k \approx 60$ –100) down to a few metres. In the original COSMO-EU data a 5/3 power law scaling seems to be present down to a wavelength range of 30 km.

Next a new Fourier spectrum is constructed from the large scale amplitudes (up to $k = 80$) with small scale amplitudes (smaller than 30 km) obtained according to a 5/3 power law up to wavenumbers of $k = 486$ (according to a wavelength of 2×2.33 km). Using these new amplitudes (and related random phases) a new 2-D field of liquid water content for this layer is constructed by a backward Fourier transform on an increased horizontal resolution (Fig. 1c). As this new fields does not obey the original liquid water content on 7 km resolution each Fourier step is followed by a step restoring this requisite. Figure 1e shows the resulting field of liquid water content after 3 iteration steps. The Fourier spectrum is not perfect (Fig. 1f) due to the requirement of conserving the 7 km COSMO-EU-scale LWC distribution. This introduces discontinuities as the cloud gaps and also the block structure reflecting the original resolution. Nonetheless, a field matching the COSMO-EU weather model cloud physics on COSMO-EU resolution comprising statistically realistic small scale variability is generated.

Finally, atmospheric profiles from the COSMO-EU are extended to 120 km using the standard AFGL midlatitude summer atmosphere (Anderson et al., 1986). Trace gases not contained in the COSMO-EU output, in particular ozone, are also taken from this standard profile.

All final input fields have thus a resolution of 2.33 km and are given on a $972 \times 972 \times 50$ grid. This way a scene of the size of Central Europe is generated with large structures of real weather related cloudiness and realistic detail on the small scales. In general such a resolution could as well be achieved by utilising the high-resolution COSMO-DE. However such a model run alone would not produce realistic variability on the smallest model scales either due to numerical diffusion. In addition to that, inevitably, the domain size had to be much smaller due to computational limits.

Validation of retrievals with simulated data

L. Bugliaro et al.

Title Page

Abstract

Introduction

Conclusions

References

Tables

Figures



Back

Close

Full Screen / Esc

Printer-friendly Version

Interactive Discussion



3.1.3 Microphysics

Once resolution has been enhanced, cloud microphysics has to be associated to the cloud liquid and ice water fields. For water clouds liquid water content LWC [kg/m³] and effective radius $r_{\text{eff}} = \int r^3 n(r) dr / \int r^2 n(r) dr$ [μm] ($n(r)$ is the particle size distribution in droplets/m³) are connected through

$$r_{\text{eff}} = \left(0.75 \cdot \left(\frac{\text{LWC}}{\pi \cdot k \cdot N \cdot \rho} \right) \right)^{1/3} \times 10^{-6}. \quad (1)$$

Water droplet density N [1/m³] must be given (here = 150.0e6 1/m³) and is kept constant for all clouds in the domain. The k factor describes the ratio between the volumetric radius of droplets, i.e. the mean volume radius, $r_v = (\int n(r) r^3 dr / \int n(r) dr)^{1/3} = (\int n(r) r^3 dr / N)^{1/3}$ and their effective radius r_{eff} : $k = r_v^3 / r_{\text{eff}}^3$ and varies between 0.67 ± 0.07 for continental clouds and 0.8 ± 0.07 for marine clouds according to Martin et al. (1994). Here we used a typical value of $k = 0.75$. ρ is water density at 4° C in kg/m³.

For ice clouds the parameterisation of randomly oriented hexagonal columns by (Wyser and Ström, 1998; McFarquhar et al., 2003) is used which relates ice particle effective radius r_{eff} [μm] to ice water content IWC [kg/m³] and temperature T [K]:

$$b = -2.0 + 0.001 \cdot (\sqrt{273 - T})^3 \cdot \log((\text{IWC}/1000)/(50 \text{ g/m}^3))$$

$$r_0 = 377.4 + 203.3 \cdot b +$$

$$37.91 \cdot b^2 + 2.3696 \cdot b^3$$

$$n_{ft} = (\sqrt{3} + 4)/(3\sqrt{3})$$

$$r_1 = r_0/n_{ft}$$

$$r_{\text{eff}} = (4\sqrt{3}/9)r_1$$

Validation of retrievals with simulated data

L. Bugliaro et al.

Title Page

Abstract

Introduction

Conclusions

References

Tables

Figures

◀

▶

◀

▶

Back

Close

Full Screen / Esc

Printer-friendly Version

Interactive Discussion



3.2 Radiative transfer model

In order to simulate satellite images from forecast model fields, a radiative transfer forward model needs to be applied. We take advantage of the libRadtran package (<http://www.libradtran.org>) which has been jointly developed since more than 10 years by Bernhard Mayer (Deutsches Zentrum für Luft- und Raumfahrt, DLR, and Ludwig Maximilians University in Munich, LMU), Arve Kylling (formerly NILU, Norway), and recently Ulrich Hamann (DLR), Claudia Emde and Robert Buras (LMU). libRadtran (Mayer and Kylling, 2005) provides a flexible interface to address all kinds of questions, and to compute irradiances (fluxes), actinic fluxes, radiances (intensities) and heating rates. Different methods are implemented, to calculate at very high spectral resolution (line-by-line), at intermediate resolution (suited to simulate satellite instruments) and for integrated solar and thermal irradiances and radiances. It has been validated in several model intercomparison campaigns, and by direct comparison with observations (e.g., Mayer et al., 1997; Van Weele et al., 2000; DeBacker et al., 2001). Particular attention has been laid on the detailed and most realistic representation of water and ice clouds in the model. Optical properties of water droplets are computed using Mie theory and tabulated as a function of wavelength and effective radius. Ice crystals must not be assumed to be spherical particles and need therefore a special treatment since the conversion from microphysical to optical properties is much less defined. For this simulation the parameterisation of Key et al. (2002) and Yang et al. (2000) for hexagonal ice columns has been selected since it has an adequate spectral resolution. However, it only covers the solar spectral bands of MET-8/SEVIRI. Thus, starting from new single scattering optical properties provided by P. Yang (personal communication, 2006), we have developed a new parameterisation covering the complete solar and thermal spectral range between 0.25 and 100 μm , consistent with that of Key et al. (2002) and Yang et al. (2000) for the solar part of the spectrum. The resulting parameterisation of ice crystal optical properties is thus consistent over the full MET-8/SEVIRI spectral range (Fig. 3). Aerosols also deserved a comprehensive treatment. As default we used the

Validation of retrievals with simulated data

L. Bugliaro et al.

Title Page

Abstract

Introduction

Conclusions

References

Tables

Figures



Back

Close

Full Screen / Esc

Printer-friendly Version

Interactive Discussion



rural aerosol model by Shettle (1989) in the boundary layer, background aerosol above 2 km, spring-summer conditions and a visibility of 50 km.

The selected one-dimensional radiative transfer solver is DISORT 2.0 by Stamnes et al. (1988, 2000), with 16 streams. Atmospheric gas absorption has been adopted from SBDART (Ricchiuzzi et al., 1998) and relies on low resolution band models developed for the LOWTRAN 7 atmospheric transmission code (Pierluissi and Peng, 1985). It uses an exponential sum fit with a resolution of 20 cm^{-1} . We adopted 15 spectral grid points to simulate each low resolution channel. The HRV channel was not simulated.

3.3 Surface

The underlying surface is described in terms of a Lambertian spectral albedo taken from the MODIS albedo product MOD43C1 (Schaaf et al., 2002) for the year 2004 and the Julian day 225 for the area corresponding to the COSMO-EU region and the 7 solar MODIS channels contained in the spectral range 460 nm–2155 nm for which albedo has been derived. From MODIS thermal channels emissivity is derived by the MODIS land surface team and made publicly available in form of the MOD11C2 product (Wan and Li, 1997). For the year 2004 and the Julian day 225 emissivities for wavelengths around 3.9, 8.7, 10.8 and $12.0 \mu\text{m}$ have been extracted from the appropriate product, transformed into albedos ($\text{emissivity} = 1 - \text{albedo}$) and gathered into spectral albedo files for every resolution enhanced COSMO-EU pixel.

Albedo values are interpolated linearly between MODIS channels and assumed constant below 460 nm and above $12.3 \mu\text{m}$. For water bodies, surface albedo was computed in clear sky conditions for all MET-8/SEVIRI solar channels by using the ocean BRDF by Nakajima and Tanaka (1983) and Cox and Munk (1954a,b). These values were then again collected into a spectral albedo file and used as input to the radiative transfer simulations.

Examples of the resulting albedos and emissivities are given in Fig. 4.

Validation of retrievals with simulated data

L. Bugliaro et al.

Title Page

Abstract

Introduction

Conclusions

References

Tables

Figures



Back

Close

Full Screen / Esc

Printer-friendly Version

Interactive Discussion



3.4 Solar and viewing geometry

Solar zenith angles, satellite zenith angles and relative azimuth angles between sun and satellite have been produced for the geographic location of every COSMO-EU pixel in higher resolution, i.e. after downscaling. Sun zenith angle lies in the range 25.1°–48.5° (mean value = 36.5°), satellite zenith angle in the range 45.1°–72.0° (mean value = 58.6°), relative azimuth angle in the range 0.0°–12.2° (mean value = 4.5°). The satellite selected is MET-8 (MSG-1) located at –3.4° E, which was its operational orbit position until April 2008.

4 Simulations

Starting from the datasets and the radiative transfer model described in Sect. 3 radiances for every MET-8/SEVIRI channel have been computed. Two examples, the solar channel VIS008 and the thermal water vapour channel WV_062, are shown in Fig. 5.

To take into account the misleading definition of spectral radiance in the thermal range (eum, 2007) used by EUMETSAT's Meteorological Product Extraction Facility for the processing of the Meteosat Second Generation data, an algorithm has been written that transforms the correct spectral radiances (also called effective spectral radiances in the mentioned EUMETSAT document) produced by the radiative transfer model into spectral radiances (i.e. at a defined wavenumber) as they are expected by most algorithms for the detection of clouds that have been tuned and tested with real data so far.

After this correction radiances are convolved with the instrument point spread function and brought into MET-8/SEVIRI projection by averaging all model values that belong to a given satellite pixel.

The resulting MET-8/SEVIRI area simulated in this study thus comprises elements 1335 to 2111 and lines 3132 to 3536 in native coordinates (i.e. from the South-Eastern corner of the MET-8 disc where the SEVIRI spinning radiometer starts scanning the Earth).

Validation of retrievals with simulated data

L. Bugliaro et al.

Title Page

Abstract

Introduction

Conclusions

References

Tables

Figures

◀

▶

◀

▶

Back

Close

Full Screen / Esc

Printer-friendly Version

Interactive Discussion



and spatial coherence tests. The last test group aims at cirrus clouds alone: a cirrus cloud is detected when at least one of the cirrus tests described in Krebs et al. (2007) gives a positive result. This day and night cirrus algorithm consists of six sub-tests based on the infrared SEVIRI channels alone that exploit spectral as well as morphological properties of cirrus clouds.

Threshold values used in the tests are either determined empirically, or derived from clear-sky albedo maps applying an atmospheric and viewing angle correction, or they are obtained from NWP (ECMWF) data by means of the libRadtran radiative transfer model (see also following Sect. 5.1.2).

5.1.2 Cloud top height

In order to infer cloud top height (i.e. pressure and temperature) two techniques are used: for opaque clouds, the measured IR₁₀₈ window channel brightness temperature is matched against a collocated atmospheric temperature profile obtained from ECMWF analysis data. In the case of semi-transparent or sub-pixel clouds, however, this technique fails and the CO₂ slicing method is used where infrared channel radiances at IR₁₀₈ and at IR₁₃₄ for black clouds located at different layers of the atmosphere are ratioed (Cayla and Tomassini, 1978; Szejwach, 1982; Nieman et al., 1993; Menzel et al., 1983; Schmetz et al., 1993). For both methods atmospheric profiles of temperature, pressure, water vapour and ozone are taken from ECMWF analyses with a 0.25°×0.25° spatial resolution in longitude and latitude. Then, they are input to libRadtran to simulate TOA radiances from black clouds located at different levels in the atmosphere. The vertical grid chosen here sets black cloud tops from the surface to 15 km altitude in 1 km steps.

5.1.3 Cloud top phase

Ice clouds are observed when the cirrus detection results by Krebs et al. (2007) are positive, i.e. when a cirrus has been detected. All other clouds are classified as liquid water clouds.

Validation of retrievals with simulated data

L. Bugliaro et al.

Title Page

Abstract

Introduction

Conclusions

References

Tables

Figures

◀

▶

◀

▶

Back

Close

Full Screen / Esc

Printer-friendly Version

Interactive Discussion



5.1.4 Cloud optical thickness and effective radius

Two channels are used for the determination of cloud optical thickness and cloud effective radius: VIS006 (without water or ice absorption, respectively) and IR_016 (with water or ice absorption). The algorithm is based on the method described by Nakajima and King (1990) and Nakajima and Nakajima (1995), but has been adapted to MET-8/SEVIRI in order to make use of the two solar channels instead of the three classical channels. Comparison of pre-calculated values of the reflectivities with corresponding measured quantities yields the optical thickness and effective radius that best reproduce the measurements. For this purpose, reflectivities are tabulated in advance with libRadtran as a function of the relevant parameters (sun zenith angle, sensor zenith angle, relative azimuth angle, surface albedo, cloud optical thickness, and effective particle radius). Water cloud effective radii run from 5 to 25 μm while ice cloud effective radii are in the range 6–84 μm . Water cloud optical properties are computed according to Mie theory, while ice cloud optical properties are parameterised after Key et al. (2002); Yang et al. (2000). In particular, r_{eff} for ice particles equals $\frac{3}{4}V/A$, where V is the total volume of the particles and A is the total projected area. Information about surface albedo over land is extracted from the MODIS white albedo product MCD43C3 with a 0.05° spatial resolution for MODIS bands 1 (620–670 nm) and 6 (1628–1652 nm).

5.2 CMSAF

As a second test retrieval we selected the operational software used by the Climate Monitoring Science Application Facility (CMSAF) for the creation of long term data sets of cloud properties. It consists of two parts: the first one includes the SAFNWC/MSG version1.4 (2008) software developed by METEO FRANCE (Derrien and LeGleau, 2005; SAFNWC, 2007) in the framework of the Science Application Facility for Now-casting (SAFNWC): in this study we used the products PGE01 (cloud mask) and PGE03 (cloud top temperature). The second part consists in the cloud physical product retrieval CPP from Roebeling et al. (2006) and Meirink et al. (2010) that derives cloud optical thickness and cloud water path.

Validation of retrievals with simulated data

L. Bugliaro et al.

Title Page

Abstract

Introduction

Conclusions

References

Tables

Figures

◀

▶

◀

▶

Back

Close

Full Screen / Esc

Printer-friendly Version

Interactive Discussion



5.2.1 Cloud detection

The algorithm is based on multispectral threshold techniques applied to each pixel and works in four steps. In the first step, a series of tests allows the identification of pixels contaminated by clouds or snow/ice. Similarly to APICS, reflectance tests, temperature tests, temperature difference tests, and spatial coherence tests are applied. Most thresholds are determined from sun- and satellite-dependent look-up tables and make use of NWP forecast fields (surface temperature and total atmospheric water vapour content) and ancillary data (elevation and climatological data) from the GME model (Majewski, 1998; Majewski et al., 2002) with a resolution of $0.5^\circ \times 0.5^\circ$ in latitude and longitude. These thresholds are computed at a spatial resolution of 16×16 pixels. The second step allows on one side to reclassify pixels having a class type different from their neighbours. On the other side, an opacity and a complete overcast cloud flag is extracted for all cloud contaminated pixels. The third step consists in the assessment of the quality of the cloud detection process, while the last step identifies dust clouds and volcanic ash clouds and is applied to all pixels. More details can be found in (SAFNWC, 2007).

5.2.2 Cloud top height

The basis for cloud top height retrievals are simulated vertical profiles of cloud free and overcast radiances and brightness temperatures for the thermal SEVIRI channels WV_062, WV_073, IR_134, IR_108 and IR_120. They are computed with the RTTOV-7 radiative transfer model (Saunders et al., 2002) applied to NWP temperature and humidity vertical profiles with a horizontal spatial resolution of 32×32 SEVIRI pixels. For opaque clouds, the cloud top pressure corresponds to the best fit between the simulated and the measured IR_108 brightness temperatures. In the case of semi-transparent or sub-pixel clouds two bi-spectral techniques are used instead: first, the H₂O intercept method is applied sequentially to a window (IR_108) and a sounding (IR_134, WV_073, WV_062) channel. In its original formulation, it exploits the fact that

Validation of retrievals with simulated data

L. Bugliaro et al.

Title Page

Abstract

Introduction

Conclusions

References

Tables

Figures

◀

▶

◀

▶

Back

Close

Full Screen / Esc

Printer-friendly Version

Interactive Discussion



water vapour radiances vary linearly against IR window radiances as a function of cloud amount to extrapolate the correct cloud height (see references in Sect. 5.1.2). The final retrieved cloud top pressure is the averaged cloud top pressure obtained using single sounding channels. If this first step fails, the radiance ratioing method, adapted from the CO₂ slicing by (Smith et al., 1970; Chahine, 1974; Smith et al., 1974; Smith and Platt, 1978; Menzel et al., 1983; Eyre and Menzel, 1989; Nieman et al., 1993), is applied successively to the window IR_108 and the sounding channels WV_073, WV_062 and IR_134 until a result is obtained. In case this result is warmer than the corresponding IR_108 brightness temperature, the method for opaque clouds is used instead.

5.2.3 Cloud top phase, cloud optical thickness and cloud effective radius

The method iteratively interprets reflected solar radiation in the VIS006 and IR_016 channels in terms of cloud top phase, cloud optical thickness and cloud effective radius. The physical basis for the determination of optical thickness and effective radius is the same as in Nakajima and King (1990) and Nakajima and Nakajima (1995): they are obtained by simultaneously comparing satellite observed reflectances at visible and near-infrared wavelengths to look-up tables of simulated reflectances. In addition the method exploits the fact that at 1.6 μm the imaginary index of refraction is higher for ice particles than for liquid particles to infer cloud phase (see for instance Baum et al. (2000)).

The algorithm, described in Roebeling et al. (2006), starts with retrieving a cloud optical thickness at 0.6 μm that is used to update the retrieval of particle size at 1.6 μm. This iteration process initially assumes ice clouds and continues until the retrieved cloud physical properties converge to stable values. In this case, infrared cloud emissivity is computed from the optical thickness according to (Minnis et al., 1993), and this quantity is used to correct the 10.8 μm brightness temperature and obtain cloud top temperature. If this is lower than 265 K, ice phase is maintained, otherwise the iteration scheme is started from scratch again assuming liquid water clouds. Finally, for optically thin clouds (optical thickness <8) the retrieved particle sizes are reset to

Validation of retrievals with simulated data

L. Bugliaro et al.

Title Page

Abstract

Introduction

Conclusions

References

Tables

Figures



Back

Close

Full Screen / Esc

Printer-friendly Version

Interactive Discussion



climatological values of 8 μm for water and 26 μm for ice clouds, values close to those used by (Rossow and Schiffer, 1999). To obtain a smooth transition between assumed and retrieved effective radii a weighting function is applied to the effective radii of cloudy pixels with optical thickness between zero and eight.

5 The Doubling-Adding KNMI (DAK) monochromatic radiative transfer model (de Haan et al., 1987; Stammes, 2001) is used to compile the required look-up tables. To translate line reflectances into SEVIRI channel reflectances, line-to-band conversion coefficients are computed by convolving Scanning Imaging Absorption Spectrometer for Atmospheric Chartography (SCIAMACHY, aboard the european research satellite EN-
10 VISAT, Stammes et al., 2005) spectra with the SEVIRI spectral response functions (Roebeling et al., 2006). For water clouds optical properties are obtained from Mie theory for effective radii (Hansen and Travis, 1974) between 1 and 24 μm ; for ice clouds a homogeneous distribution of Cb, C1, C2 and C3 type imperfect hexagonal ice crystals from (Hess et al., 1998) is used with volumetric radii r_v of 6, 12, 26 and 51 μm respectively (see Sect. 3.1.3 for the definition of this radii).

Cloud top phase corresponds to the resulting phase used in the τ - r_{eff} retrieval (Wolters et al., 2008).

20 Unlike in the operational chain at CMSAF, the algorithm is run here without recalibrating the solar channels to take into account the fact that simulated radiances are exact.

5.2.4 Cloud water path

Cloud water path CWP is derived from retrieved cloud optical thickness τ and droplet effective radius r_{eff} (see Sect. 5.2.3) by means of the relation (Stephens, 1978):

$$\text{CWP} = \frac{2}{3} \tau r_{\text{eff}} \rho_l, \quad (2)$$

25 where ρ_l is the density of liquid water. Equality holds true when the size parameter $2\pi r/\lambda$ is large enough such that scattering efficiency can be approximated with a value

Validation of retrievals with simulated data

L. Bugliaro et al.

Title Page

Abstract

Introduction

Conclusions

References

Tables

Figures

◀

▶

◀

▶

Back

Close

Full Screen / Esc

Printer-friendly Version

Interactive Discussion



of 2. This is only completely correct for water clouds and under the assumption that the cloud has a constant effective radius vertical profile. The CPP algorithms first computes optical thickness τ and effective radius r_{eff} and then derives cloud water path according to the above equation. Although in the CMSAF processing chain only optical thickness and cloud water path are output, in this case effective radius was added to the output list.

6 Validation

Validation of cloud properties derived from satellite data is a complicated issue. Commonly, either surface and airborne measurements are used, or intercomparisons of space-borne retrievals are performed in order to identify their strengths and weaknesses. However, only few in-situ data are available for the validation of quantities like cloud phase or particle size, or the combination of numerous instruments is required. The major challenge consists in the different scales and different samplings of these measurements such that inherent discrepancies may exist that prevent the assessment of the performance or uncertainty of the satellite retrieval (e.g. Schutgens and Roebeling, 2009). Thus, cloud properties retrieved from space-borne algorithms can only be partially validated at distinct points in space (and time) by means of surface or airborne measurements. In addition, three dimensional radiative effects and cloud inhomogeneity have been shown to introduce bias and considerable noise into the retrieved optical thickness and effective radius (Zinner and Mayer, 2006). Noise in particular precludes the use of in-situ observations when no statistically significant result can be achieved due to the usually limited availability of such data sets or to the rarity of satellite overpasses over the validation sites.

When comparing satellite retrievals with each other interesting aspects can be identified and some light can be shed on the “true” cloud properties by considering the agreement or disagreement of the retrievals. Nevertheless, this does not enable at all a quantitative validation of the derived cloud properties.

Validation of retrievals with simulated data

L. Bugliaro et al.

Title Page

Abstract

Introduction

Conclusions

References

Tables

Figures



Back

Close

Full Screen / Esc

Printer-friendly Version

Interactive Discussion



Validation of retrievals with simulated data

L. Bugliaro et al.

Title Page

Abstract

Introduction

Conclusions

References

Tables

Figures

⏪

⏩

◀

▶

Back

Close

Full Screen / Esc

Printer-friendly Version

Interactive Discussion



Here we show a paradigmatic validation of the two space-borne cloud retrievals APICS and CMSAF by means of the satellite scene simulated for MET-8/SEVIRI as explained in Sects. 4 and 5. This enables an objective validation of the algorithms since all the components of the Earth-atmosphere system that lead to the “observed” satellite radiances are known and can be directly compared to the output fields of the retrieval algorithms.

In the following we will denote by “retrieved” all the cloud properties that are output of the satellite retrievals. In contrast, the word “real” or “reality” will be used to characterise those cloud properties that stem from the COSMO-EU weather model, have been subsequently downscaled and finally used as input to the radiative transfer model for the simulation of the satellite scene. In fact, these are the cloud properties that lead to the radiance fields used in this study.

To make a comparison of retrieved and real cloud properties possible, real cloud properties have been projected to MET-8/SEVIRI grid in a similar way as the simulated radiances (see Sect. 4). More details will be given in the next subsections when cloud mask (Sect. 6.1), cloud top temperature (Sect. 6.3), cloud top phase (Sect. 6.2), cloud optical thickness (Sect. 6.4), cloud water path (Sect. 6.6) and cloud effective particle radius (Sect. 6.5: here a statistics over all cloud boxes inside a given MET-8/SEVIRI pixel is reported) will be addressed. However, Table 2 summarises all relevant real cloud properties of concern.

6.1 Cloud detection

Reality is represented in this case by the projection of the real binary (0/1) cloud mask originally defined on the downscaled COSMO-EU grid onto the MET-8/SEVIRI grid. This first yields a cloud cover mask from which a cloud mask has been obtained: all MET-8/SEVIRI pixels with cloud cover larger than zero have been defined to be cloudy.

The APICS retrieval yields directly a binary cloud mask, while more than one CMSAF output field has been combined into a cloud mask. First, the PGE01 product flags for “cloud contaminated” and “cloud filled” pixels were used to identify cloudy pixels.

Second, the corresponding CMSAF dust and volcanic ash detection products were considered in order to cleanse the cloud mask from these spurious contaminations (which in this case were almost nonexistent). Finally, the CMSAF cloud mask quality flag was used to select only high confidence pixels. This provides us with two retrieved cloud masks that can be validated against the real cloud mask.

The discrepancies between APICS and real cloud mask as well as between CMSAF and real cloud mask are plotted in Fig. 7a and b. It can be immediately noticed that the two retrieved cloud masks are similar to each other. In fact, both cloud detection schemes prove their capability to reproduce the input cloud distribution. Anyway, differences between the two algorithms are present and missing knowledge about the real cloud distribution in the observed domain could lead to erroneous conclusions. For instance, one can see in the South-Western part of the picture that no retrieval is able to detect the edges of the cloud field (the coincident red colour in the cloud mask difference plots). On the contrary, some pixels are retrieved as overcast by both retrievals while in reality they are not (the turquoise colour).

In order to quantitatively assess the performance of the cloud detection algorithms, we evaluate various quantity including the Hanssen-Kuiper (HK) skill score (Hanssen and Kuipers, 1965), also called true skill score, applied to the pixels of the simulated scene. This measure is often used to evaluate the skill of precipitation forecasts (see Tartaglione (2010) and references therein) but also of cloud detection schemes (Reuter et al., 2009). The HK skill score is based on the 2x2 contingency table of the detection events (Table 3). The four elements of the table are the hit a , false alarm b , miss c , and correct negative events d . The HK score, defined as

$$HK = \frac{ad - bc}{(a+b)(c+d)} = \frac{d}{c+d} + \frac{a}{a+b} - 1, \quad (3)$$

is independent of the distribution of events (really cloudy pixels) and nonevents (really cloud free pixels) (Woodcock, 1976), and can be expressed as the sum of the accuracy for events (probability of cloud detection, first term in Eq. 3) and the accuracy of nonevents (probability of cloud free detection, second term in Eq. 3) plus -1 to ensure

Validation of retrievals with simulated data

L. Bugliaro et al.

Title Page

Abstract

Introduction

Conclusions

References

Tables

Figures

◀

▶

◀

▶

Back

Close

Full Screen / Esc

Printer-friendly Version

Interactive Discussion



that $-1 \leq HK \leq 1$. An HK score equal to 1 is associated with a perfect cloud detection ($b = c = 0$), while a score of -1 means that hits and correct negatives are zero ($a = d = 0$). The HK score is equal to 0 for a constant forecast (either $a = c = 0$ or $b = d = 0$).

5 Considering first APICS (Fig. 7a), four features are observable: 1) an extended cloud field is detected in the North-Eastern corner of the simulation which is actually much smaller; 2) some coastlines are classified as clouds; 3) many of the cloud border pixels, with fractional cloud cover, are not detected; 4) some mistakenly detected cloud over the Alps. In more detail, the domain considered contains 254 184 pixels, 156 135 are cloudy and the remaining 98 049 are clear. The retrieval output and the real cloud mask both contain a cloud in 144 830 pixels, i.e. 93% of all cloudy pixels have been detected. Only $\approx 7\%$ of the cloudy pixels have not been detected (11 305 pixels), while the false alarm rate (clear pixels that are retrieved as cloudy) amounts to 8%, i.e. 19 105. Unfortunately, due to the features identified above, only approximately 81% of the input clear pixels are classified accordingly by APICS. Altogether, the retrieval agrees with the reality, both clear or both cloudy, on approximately 88% of all pixels (223 774 pixels). The HK score amounts to 0.73.

10
15
20
25 Considering CMSAF, (Fig. 7b), as for APICS, some of the cloud border pixels with fractional cloud cover are not classified correctly, while in the Eastern part of the simulation some nonexistent cloud is detected. CMSAF detects 96% (149 843 pixels) of all cloudy pixels, the false alarm rate amounts to 9.5% (24 197 pixels have been mistakenly classified as cloudy). Altogether, only approximately 75% of the really clear pixels are classified as that by CMSAF (73 852 pixels). Retrieval and reality agree (both clear or both cloudy) on 88% of all pixels (223 695 pixels). The corresponding HK score is 0.71.

6.2 Cloud top phase

The real cloud top thermodynamic phase on the SEVIRI grid is computed from the original quantity on the downscaled COSMO-EU grid by “averaging” the cloud top val-

Validation of retrievals with simulated data

L. Bugliaro et al.

Title Page

Abstract

Introduction

Conclusions

References

Tables

Figures

◀

▶

◀

▶

Back

Close

Full Screen / Esc

Printer-friendly Version

Interactive Discussion



ues for all pixels belonging to the same satellite pixel. Since more cloud phases could be present in every MET-8/SEVIRI pixel after re-projection, we decided to label every pixel according to the cloud top phase that appears most frequently in that pixel.

Since retrieved and real cloud mask differ, the validation of all retrieved cloud products over every single retrieval algorithm is restricted to the pixels that are cloudy in the real as well as in the retrieved cloud mask. This new cloud mask is called common cloud mask. Since two retrieval algorithms are investigated there are two common cloud masks, one for APICS and one for CMSAF.

The common cloud mask for APICS contains 144 830 cloudy pixels. Out of them, 14 516 are real water and 130 314 real ice clouds. The APICS retrieval classifies 59% (8630 pixels) of the real water clouds as water and 99% (128 672 pixels) of the real ice clouds as ice. The large difference for water clouds (see Fig. 7a and c) is produced by the erroneous classification of the cloud field in the North-Eastern corner. Here, APICS evidently detects an extended cirrus cloud on top of the real water cloud and therefore assigns the wrong cloud top phase to these pixels. Since this cloud makes up more or less half of all real water clouds, the retrieval performance is heavily affected. Overall, reality and APICS agree for almost 95% (137 302 pixels) of all common cloud pixels.

The common cloud mask for CMSAF is composed of 145 915 cloudy pixels. Out of them, 17 620 are real water and 128 295 real ice clouds. The CMSAF retrieval classifies almost 100% (17 604 pixels) of the real water clouds as water and 76% (97 441 pixels) of the real ice clouds as ice. The large difference for ice clouds (see Fig. 7b and d) is produced by the erroneous classification of the cloud edges. Overall, reality and CMSAF algorithm agree for 79% (115 045 pixels) of all common cloud pixels.

6.3 Cloud top temperature

Cloud top temperature has a direct impact on the outgoing longwave radiation at top-of-atmosphere since it determines cloud emission. Furthermore, temperatures are directly measured by the SEVIRI sensors in its thermal channels and through this quantity height assignment is performed. Thus, the two related quantities, cloud top height

Validation of retrievals with simulated data

L. Bugliaro et al.

Title Page

Abstract

Introduction

Conclusions

References

Tables

Figures



Back

Close

Full Screen / Esc

Printer-friendly Version

Interactive Discussion



and cloud top pressure, are neglected and the focus is put on cloud top temperatures. Again, the comparison between reality and retrievals is made on the basis of the common cloud masks, regardless of the fact that some cloud pixels have been assigned the wrong thermodynamic phase since this information does not enter the computation of cloud top temperatures. Figure 7e and f show relative differences between retrieved and real cloud top temperatures for APICS and CMSAF respectively. Largest discrepancies are produced by APICS at the edges of cirrus clouds, but the overall agreement is good. The APICS mean difference is 3.1 K with a standard deviation of 10.6 K. This translates into a mean relative difference of 0.01 and standard deviation of 0.05 (the mean cloud top temperature of the real clouds investigated here is 228.8 K). This slight overestimation of cloud top temperature means that cloud tops are located lower in the atmosphere by the APICS retrieval than they are in reality. This is a usual feature of the technique employed (see Sect. 5.1.2) since it determines the height (temperature) of the “radiative centre” of the cloud (Menzel et al., 1992), which is located further down in the atmosphere.

Figure 7f shows relative differences between CMSAF and real cloud top temperatures. The box structures that can be observed stem from the coarser resolution of the NWP model used for the preparation of the ancillary data set of black cloud radiances (see Sect. 5.2.3). Largest discrepancies (underestimations) are produced here at the edges of cirrus clouds but also some water cloud temperature is underestimated. The overall agreement is good. The mean CMSAF difference is -16.4 K with a standard deviation of 37.3 K corresponding to a mean relative difference of -0.07 and standard deviation of 0.15. (The mean cloud top temperature of the real clouds investigated here is 229.9 K.) This underestimation of CMSAF cloud top temperatures is mainly produced at cloud edges. Only here, CMSAF cloud top temperatures are significantly lower than real ones while the rest of the cloudy pixels show accurate results. This effect masks the typical overestimation observed in the APICS results.

Validation of retrievals with simulated data

L. Bugliaro et al.

Title Page

Abstract

Introduction

Conclusions

References

Tables

Figures

◀

▶

◀

▶

Back

Close

Full Screen / Esc

Printer-friendly Version

Interactive Discussion



6.4 Cloud optical thickness

We restrict the validation to those pixels that belong to the common cloud masks, like in the previous sections (Sects. 6.2 and 6.3). Furthermore, we only consider a subset of this common cloud mask where both retrieved and real clouds have the same top thermodynamic phase and further distinguish between those cloudy pixels that exclusively contain either water or ice clouds on one side and those that contain water and ice clouds at the same time. In this last pixel class called multi-phase in the following various cloud situations are collected: vertically extended clouds like cumulonimbus that are made up of liquid water droplets at their base and of ice crystals at their top belong to this class as well as pixels where a water cloud and a contiguous cirrus cloud coexist as well as clouds containing mixed phase layers with both liquid water droplets and ice particles or cirrus clouds on top of liquid water clouds. This kind of clouds is outlined since it does not correspond to any of the cloud classes considered (pure water or pure ice) in the retrieval cloud optical thickness and effective radius such that larger inaccuracies are expected. The distribution of real water, ice and multi-phase clouds is shown in Fig. 8.

This leaves us with 8548 water cloud, 100 480 ice cloud and 27 444 multi-phase cloud pixels for APICS and 16 829 water cloud, 75 768 ice cloud and 22 224 multi-phase cloud pixels for CMSAF. Notice that these numbers are different from those exposed in Sect. 6.2 since we consider three classes here instead of two (see also Table 2).

Evidently, both retrievals are capable of reproducing the real distribution of cloud optical thicknesses as can be seen from Fig. 9 which depicts histograms and scatter plots of retrieved and real optical thickness.

As far as APICS is concerned, the distribution of water and ice clouds is better approximated than that for multi-phase clouds as attested in Fig. 9a–c. These panels show retrieval histograms for the pixels of the common cloud mask (red lines) and histograms of real optical thickness without restrictions to the common mask (green lines).

Validation of retrievals with simulated data

L. Bugliaro et al.

Title Page

Abstract

Introduction

Conclusions

References

Tables

Figures



Back

Close

Full Screen / Esc

Printer-friendly Version

Interactive Discussion



Validation of retrievals with simulated data

L. Bugliaro et al.

[Title Page](#)[Abstract](#)[Introduction](#)[Conclusions](#)[References](#)[Tables](#)[Figures](#)[⏪](#)[⏩](#)[◀](#)[▶](#)[Back](#)[Close](#)[Full Screen / Esc](#)[Printer-friendly Version](#)[Interactive Discussion](#)

In fact, the histogram peak around optical thickness 10 for multi-phase clouds is more pronounced in the retrieval than in reality. For water clouds, APICS misses the first peak while it overestimates the second one. Plots d–f in Fig. 9 confirm a good correlation between real and retrieved water and ice cloud optical thicknesses respectively (0.977 and 0.996). Here of course both retrieved and model results are for pixels of the common cloud mask. Altogether, APICS slightly underestimates real optical thickness: mean differences between retrieved and real cloud optical thickness amount to -0.71 for water and -0.13 for ice clouds, with a standard deviation of 1.20 for water clouds which is higher than for ice clouds (0.40). Multi-phase clouds show a worse correlation of 0.957, a mean underestimation of -6.50 and a larger scattering of 8.72. However, those multi-phase clouds that were treated as water clouds by APICS lie on the one-one line.

Finally, relative differences (Fig. 10) between optical thicknesses of real and retrieved water and ice clouds are both quite sharply peaked around -0.04 while the relative difference distribution of multi-phase clouds is much more flat with a peak around -0.45 .

Considering now CMSAF results (blue lines in Fig. 9a–c), a slightly different behaviour can be observed. While the histogram curves of retrieved and real cloud optical thickness occurrences overlap for multi-phase clouds (Fig. 9c), the water cloud distribution does not account for two peaks (Fig. 9a): real water clouds have two peaks at around optical thickness 1–2 and 7–8 while retrieved optical thicknesses are peaked in between at 2–3. For ice clouds (Fig. 9b), CMSAF underestimates the occurrence of thin clouds ($\tau \leq 2$) and overestimates the optical thickness of the remaining clouds ($\tau > 2$). Scatter plots (Fig. 9g–i) show a good one-to-one correlation for water clouds with a slight tendency to underestimation, apart from some data point whose optical thickness is overestimated by CMSAF by a factor of 2 to 5 (Fig. 9d). The effect of these limited amount of pixels is to reduce the overall accuracy of the results. The correlation coefficient between CMSAF and real water cloud optical thicknesses amounts to 0.437, the mean difference is 10.7 and the standard deviation 46.2. Mean relative difference is 0.89 with a relative standard deviation of 6.8. For ice cloud optical thickness there is a

Validation of retrievals with simulated data

L. Bugliaro et al.

Title Page

Abstract

Introduction

Conclusions

References

Tables

Figures

◀

▶

◀

▶

Back

Close

Full Screen / Esc

Printer-friendly Version

Interactive Discussion



trend towards overestimation and a correlation coefficient of 0.774. The scatter plot of CMSAF against real ice optical thicknesses in Fig. 9e also shows a structure that may be related to the four ice cloud models used in the compilation of the look-up tables for the retrieval (see Sect. 5.2.3). The mean difference of ice cloud optical thickness between CMSAF and reality amounts to 2.36 with a standard deviation of 5.0, mean relative difference is 0.80 with a similar relative standard deviation of 0.78. Multi-phase clouds (Fig. 9f) show a relatively good agreement with a tendency to overestimation as well as a large scattering (correlation coefficient=0.79, mean difference=9.40, standard deviation=36.9, mean relative difference=0.34, mean standard deviation=0.92). In particular, when the multi-phase cloud was classified as a water cloud by CMSAF, a reasonable agreement was found.

The distribution of relative differences between optical thicknesses of real and retrieved clouds is shown in Fig. 10 for CMSAF as well. Water clouds show a peak at around 0.05 while ice and multi-phase clouds present more uniform distributions that confirm the tendency to overestimation already observed in Fig. 9 and in particular the large scattering mentioned above.

Considering the different accuracies of the two (ice cloud) retrievals it must be emphasised that ice cloud properties show a relevant dependence on ice particle shape and the parameterisation of their optical properties. While APICS uses optical properties for hexagonal columns by (Key et al., 2002; Yang et al., 2000), CMSAF considers imperfect hexagonal crystals according to (Hess et al., 1998). In our reality, also (Key et al., 2002; Yang et al., 2000) was used such that APICS had a clear advantage in this case.

6.5 Cloud effective radius

Effective radius is a quantity that is particularly difficult to validate for various reasons. In reality effective radius is a function of cloud height in every pixel while space-borne retrievals usually output one single quantity since they assume the existence of homogeneous plane-parallel clouds inside every pixel. Droplet size information is contained

in the 1.6 μm MET-8/SEVIRI channel where water droplets not only reflect but also absorb solar radiation. This absorption increases with cloud droplet size: the greater the droplet absorption the less the cloud reflectance. However, these reflectances may also depend on optical thickness such that the value of the effective radius must always be determined at the same time as optical thickness which on its turn largely depends on the 0.6 μm MET-8/SEVIRI channel where absorption is marginal. However, real-world clouds are usually vertically inhomogeneous and a retrieval gives optical thickness and effective radius of a homogeneous cloud having (nearly) the same spectral reflectances as the measured one. Thus, effective radius does not only depend on the absorbing intensity of the channel used (Platnick, 2000) but is also highly retrieval dependent and there is no real truth to compare with. Nevertheless, the compilation of effective radius properties contained in Table 2 can be used to argue about some aspects of the retrieval results. The values reported there stem from a statistical evaluation of all real cloud boxes and give some information about the effective radius distribution of the real cloud: minimum, maximum and mean values of encountered r_{eff} values are listed for water, ice and multi-phase clouds.

Furthermore, while the definition of effective radius for spherical liquid water droplets after Hansen and Travis (1974) as $r_{\text{eff}} = \int r^3 n(r) dr / \int r^2 n(r) dr$ is commonly accepted ($n(r)$ being the droplet size distribution), for ice clouds various definitions are possible (see McFarquhar and Heymsfield, 1998). APICS and CMSAF use two definitions that can be mapped to each other (Schumann et al., 2010) such that a direct comparison between them is possible.

For these reasons we only show here the histograms of the two retrieval results and make some comments on their main features. Also in this case we consider the common cloud mask between the two satellite retrieval results with the additional exclusion of all the really clear pixels that have been mistakenly classified as cloudy by both algorithms (see Sect. 6.1).

Water clouds mainly contain small effective radii (see Table 2). This is mirrored in the occurrence distribution of r_{eff} as retrieved by APICS and CMSAF (Fig. 11a). Many

Validation of retrievals with simulated data

L. Bugliaro et al.

Title Page

Abstract

Introduction

Conclusions

References

Tables

Figures

◀

▶

◀

▶

Back

Close

Full Screen / Esc

Printer-friendly Version

Interactive Discussion



of the clouds but at the lower bound of the range permitted by the APICS algorithm and accumulate at $5\ \mu\text{m}$. The CMSAF algorithm also assigns many small effective radii to the clouds observed but it shows three peaks located at 3, 8 and $11\ \mu\text{m}$. The peak at $8\ \mu\text{m}$ represents those pixels with optical thickness smaller than 8 for which a (smeared) climatological value of the effective radius is used. Since the cloud does not contain any effective radii larger than $12\ \mu\text{m}$ however, retrieval results larger than this value are to be considered as unrealistic.

Ice clouds, depicted in Fig. 11b, show that APICS produces two peaks at the smallest and largest effective radius 6 and $84\ \mu\text{m}$ respectively although no cloud box is present with such a small or large effective radius (Table 2). The third APICS peak around $40\ \mu\text{m}$ instead is plausible since it is not far away from the mean effective radius $53.60\ \mu\text{m}$ averaged over all ice boxes in the domain (Table 2). One has to remind that the retrieved effective radius does not correspond to the mean effective radius of all clouds but to a weighted mean of the upper part of effective radius vertical profiles (Platnick, 2000).

CMSAF results mainly show one single higher peak at $21\ \mu\text{m}$ with a steep decrease in occurrence after this value. This again represents the climatological value $r_v = 26\ \mu\text{m}$ that corresponds to $r_{\text{eff}} = 21.41\ \mu\text{m}$ which is smeared out for clouds with optical thickness smaller than 8. This effect is stronger for ice clouds than for water clouds because there are many ice clouds with small optical thickness. No boundary effects are noticeable apart from the fact that the effective radius range retrieved by CMSAF is slightly smaller and runs approximately from 5 to $40\ \mu\text{m}$.

Multi-phase cloud show as usual a very large variability for both retrievals, but APICS again yields a large amount of clouds with $r_{\text{eff}} = 6\ \mu\text{m}$ and a sort of secondary peak at $45\ \mu\text{m}$ ca. The CMSAF retrieved effective radii have two peaks around 8–9 and $18\ \mu\text{m}$.

6.6 Cloud water path

The CMSAF retrieval is the only one that routinely generates cloud water path fields, so this quantity is analysed for the CMSAF retrieval only. Again, we restrict the validation

Validation of retrievals with simulated data

L. Bugliaro et al.

Title Page

Abstract

Introduction

Conclusions

References

Tables

Figures

◀

▶

◀

▶

Back

Close

Full Screen / Esc

Printer-friendly Version

Interactive Discussion



to those pixels that belong to the common cloud mask for CMSAF. Furthermore, like in Sects. 6.4 and 6.5 we consider the three classes of water, ice and multi-phase clouds (see Sect. 6.4 for an explanation). For CMSAF, this leaves us again with 16 828 water cloud, 75 767 ice cloud and 22 224 multi-phase cloud pixels.

5 Evidently, the retrieval is capable of reproducing the real distribution of cloud water path (Fig. 12a and c) for liquid water clouds as well as for ice clouds. However, the histogram peak around cloud water path 50 g m^{-2} for multi-phase clouds is more pronounced in the retrieval and a worse agreement is obtained. Plots on the right hand side in Fig. 12 confirm a fairly good correlation (0.672 and 0.919) between real and
10 retrieved water and ice clouds respectively. At the same time, a tendency to overestimation is shown that is reflected in the mean differences between retrieved and real cloud water path: 33.56 g m^{-2} for water and 9.62 g m^{-2} for ice clouds, with a standard deviation of 78.80 g m^{-2} for water clouds and 49.89 g m^{-2} for ice clouds. Multi-phase clouds show a correlation of 0.786, a mean overestimation of 120.10 g m^{-2} and a larger
15 scattering of 421.39 g m^{-2} .

Relative differences (Fig. 13) between cloud water paths of real and retrieved ice clouds are quite sharply peaked around 0.0. Water clouds show a shallow maximum around 0.8, while the relative difference distribution of multi-phase clouds is peaked around 0.3.

20 7 Conclusions

Based on three-dimensional cloud distributions from the COSMO-EU model and a downscaling procedure, a cloud dataset has been produced with a resolution of 2.33 km appropriate for the simulation of SEVIRI radiometer observations aboard the geostationary european MET-8 satellite (MSG-1). These clouds were input to detailed
25 bias-free one-dimensional radiative transfer calculations to produce a realistic synthetic MET-8/SEVIRI satellite scene. In this exercise, the channels were assumed to be perfectly calibrated.

Validation of retrievals with simulated data

L. Bugliaro et al.

Title Page

Abstract

Introduction

Conclusions

References

Tables

Figures



Back

Close

Full Screen / Esc

Printer-friendly Version

Interactive Discussion



Validation of retrievals with simulated data

L. Bugliaro et al.

Title Page

Abstract

Introduction

Conclusions

References

Tables

Figures

◀

▶

◀

▶

Back

Close

Full Screen / Esc

Printer-friendly Version

Interactive Discussion



The outcome of this study is a unique data set for the validation of retrieval algorithms of atmospheric, cloud, and surface properties from Meteosat Second Generation. Using the known cloud properties as a reference (i.e. as reality), we could quantitatively validate the outcome of two cloud retrieval algorithms in a closed-loop test where both input and output data sets are known.

The APICS and CMSAF cloud retrieval algorithms applied here for illustration purposes both proved to be able to satisfactorily reproduce the cloud distribution and its properties although some of them could be better retrieved than other. As far as cloud detection is concerned, APICS largest inaccuracy consisted in a misclassified (i.e. inexistent) cirrus cloud field while the CMSAF algorithm had difficulties when dealing with cloud edges.

Cloud top temperatures could also be retrieved in a correct way throughout but a large variability was shown. For instance, APICS overestimated some cirrus cloud edges while it underestimated some other cirrus field. CMSAF instead underestimated the same cirrus cloud edges and also some water clouds.

For cloud optical thickness one has to differentiate between water and ice clouds. For water clouds, where the underlying optical properties were parameterised according to Mie, a good agreement between reality and retrieval was observed, although CMSAF's scattering was slightly larger than APICS'. For ice clouds, where assumptions about shape and composition are difficult to make, the agreement between reality and model was worse. APICS, that uses the same ice optical properties parameterisation "as the real clouds", had a strong advantage and reproduced ice optical thicknesses fairly well but with a tendency to underestimation. CMSAF uses instead another parameterisation for ice crystal optical properties and overestimated real optical thicknesses. Cloud pixels containing water and ice clouds turned out, as expected, to show the largest inaccuracies and the largest scattering of results for both retrievals.

Cloud particle effective radius is difficult to evaluate since it changes with height inside real clouds while retrieval algorithms assume the cloud to have one effective radius. Thus, the validation was restricted to a plausibility check starting from the

Validation of retrievals with simulated data

L. Bugliaro et al.

[Title Page](#)[Abstract](#)[Introduction](#)[Conclusions](#)[References](#)[Tables](#)[Figures](#)[Back](#)[Close](#)[Full Screen / Esc](#)[Printer-friendly Version](#)[Interactive Discussion](#)

knowledge about the effective radius of the single real cloud boxes. The APICS retrieval tends to retrieve too small particles while the largest effective radii could fit the reality. CMSAF shows first a pronounced dependence on the climatological values that are used when the retrieved cloud has an optical thickness smaller than 8. Second, it produces some water cloud with unrealistically large effective radius while ice cloud effective particle radii seem to be underestimated.

Cloud water path was validated for CMSAF only since APICS does not provide any such information. The CMSAF retrieval proved to be particularly effective for ice clouds while for water clouds a bias could be observed. Since this product is a combination of the previous two (optical thickness and effective radius) this behaviour can be explained by comparison with the previous results.

Finally, note that since retrieval algorithms are often tuned by the actual satellite observations, including for instance their calibration biases, their performance when applied to real data could be better than when applied to the bias-free simulations produced in this study.

In summary, we have shown the potential of this method for the evaluation of space-borne algorithms and recommend its usage to the scientific retrieval community as one possible effective way to test and tune algorithms. Conceivable applications range from the quantitative evaluation of satellite algorithms as shown here to investigations about the impact of the NWP model used in the retrieval to studies about the uncertainty of calibration accuracy on the retrieved (cloud) properties to implications of point spread functions for space-borne retrievals. In future, when extensive three-dimensional satellite scene simulations will be at our disposal, also the effect of the one-dimensional radiative transport assumptions usually made in the retrievals could be investigated. Furthermore, by simulating the same scene from the point of view of a polar orbiting and a geostationary satellite synergistic effects could be examined in a detailed quantitative way.

Acknowledgements. The study was funded by the Satellite Application Facility on Climate Monitoring (CM-SAF) which is hosted by Deutscher Wetterdienst (DWD). We thank Arnold Tafferner (DLR) for careful reading of the manuscript and valuable comments.

References

- 5 Anderson, G., Clough, S., Kneizys, F., Chetwynd, J., and Shettle, E.: AFGL Atmospheric Constituent Profiles (0-120 km), Tech. Rep. AFGL-TR-86-0110, AFGL (OPI), Hanscom AFB, MA 01736, 1986. 21939
- Baum, B., Soulen, P., Strabala, K., King, M., Ackerman, S., Menzel, W., and Yang, P.: Remote sensing of cloud properties using MODIS airborne simulator imagery during SUCCESS. 2. Cloud thermodynamic phase, *J. Geophys. Res.*, 105, 11781–11792, 2000. 21948
- 10 Cayla, F. and Tomassini, C.: Détermination de la température des cirrus semitransparents, *La Météorologie*, 15, 63–67, 1978. 21945
- Chahine, M.: Remote sounding of cloudy atmospheres, I, The single cloud layer, *J. Atmos. Sci.*, 31, 233–243, 1974. 21948
- 15 Cox, C. and Munk, W.: Measurement of the roughness of the sea surface from photographs of the sun's glitter, *J. Opt. Soc. Am.*, 44, 838–850, 1954a. 21942
- Cox, C. and Munk, W.: Statistics of the sea surface derived from sun glitter, *J. Mar. Res.*, 13, 198–227, 1954b. 21942
- Davis, R.: Comparison of modeled to observed global irradiance, *J. Appl. Meteorol.*, 35, 192–201, 1996. 21937, 21938
- 20 de Haan, J. F., Bosma, P. B., and Hovenier, J. W.: The adding method for multiple scattering calculations of polarized light, *Astronomy and Astrophysics*, 183, 371–391, 1987. 21949
- DeBacker, H., Koepke, P., Bais, A., de Cabo, X., Frei, T., Gillotay, D., Haite, C., Heikkilä, A., Kazantzidis, A., Koskela, T., Kyrö, E., Lapeta, B., Lorente, J., Masson, K., Mayer, B., Plets, H., Redondas, A., Renaud, A., Schauburger, G., Schmalwieser, A., Schwander, H., and Vanicek, K.: Comparison of measured and modelled UV indices, *Meteorol. Appl.*, 8, 267–277, 2001. 21941
- 25 Derrien, M. and LeGleau, H.: MSG/SEVIRI cloud mask and type from SAFNWC, *Int. J. Remote Sens.*, 26, 4707–4732, 2005. 21946

Validation of retrievals with simulated data

L. Bugliaro et al.

Title Page

Abstract

Introduction

Conclusions

References

Tables

Figures

◀

▶

◀

▶

Back

Close

Full Screen / Esc

Printer-friendly Version

Interactive Discussion



Validation of retrievals with simulated data

L. Bugliaro et al.

Title Page

Abstract

Introduction

Conclusions

References

Tables

Figures

◀

▶

◀

▶

Back

Close

Full Screen / Esc

Printer-friendly Version

Interactive Discussion



- EUMETSAT: A Planned Change to the MSG Level 1.5 Image Product Radiance Definition, Technical Notes EUM/OPS-MSG/TEN/06/0519, EUMETSAT, 2007. 21943
- Eyre, J. and Menzel, P.: Retrieval of Cloud Parameters from Satellite Sounder Data: A Simulation Study, *J. Appl. Meteorol.*, 28, 267–275, 1989. 21948
- 5 Hansen, J. and Travis, L.: Light scattering in planetary atmospheres, *Space Sci. Rev.*, 16, 527–610, 1974. 21949, 21959
- Hanssen, A. W. and Kuipers, W.: On the relationship between the frequency of rain and various meteorological parameters, *Koninklijk Ned. Meteor. Instit., Meded. Verhand.*, 2–15, 1965. 21952
- 10 Hess, M., Koepke, P., and Schult, I.: Optical properties of aerosols and clouds: the software package OPAC, *B. Am. Meteorol. Soc.*, 79, 831–844, 1998. 21949, 21958
- Key, J., Yang, P., Baum, B., and Nasiri, S.: Parameterization of shortwave ice cloud optical properties for various particle habits, *J. Geophys. Res.*, 107(D13), 4181, doi:10.1029/2001JD000742, 2002. 21941, 21946, 21958
- 15 Krebs, W., Mannstein, H., Bugliaro, L., and Mayer, B.: Technical note: A new day- and night-time Meteosat Second Generation Cirrus Detection Algorithm MeCiDA, *Atmos. Chem. Phys.*, 7, 6145–6159, doi:10.5194/acp-7-6145-2007, 2007. 21945
- Kriebel, K.-T., Gesell, G., Kästner, M., and Mannstein, H.: The cloud analysis tool APOLLO: improvements and validation, *Int. J. Remote Sens.*, 24, 2389–2408, 2003. 21944
- 20 Lutz, H.-J.: Cloud processing for Meteosat Second Generation, Tech. memo. 4, EUMETSAT Tech. Department, 1999. 21944
- Lutz, H.-J.: Scenes analysis from MODIS and Meteosat observations, in: Proceedings of The 2002 EUMETSAT Meteorological Satellite Data Users' Conference, 2002. 21944
- Lutz, H.-J., Inoue, T., and Schmetz, J.: Comparison of split-window and a multi-spectral cloud classification for MODIS observations, *Journal of the Meteorological Society of Japan*, 81, 623–631, 2003. 21944
- 25 Majewski, D.: The new global icosahedral-hexagonal grid point model GME of the Deutscher Wetterdienst, in: Recent developments in numerical methods for atmospheric modelling, ECMWF, Seminar Proceedings, 173–201, 1998. 21947
- 30 Majewski, D., Liermann, D., Prohl, P., Ritter, B., Buchhold, M., Hanisch, T., Paul, G., Wergen, W., and Baumgardner, J.: The Operational Global Icosahedral-Hexagonal Gridpoint Model GME: Description and High-Resolution Tests, *Mon. Weather Rev.*, 130, 319–338, 2002. 21947

Validation of retrievals with simulated data

L. Bugliaro et al.

Title Page

Abstract

Introduction

Conclusions

References

Tables

Figures

◀

▶

◀

▶

Back

Close

Full Screen / Esc

Printer-friendly Version

Interactive Discussion



- Martin, G., Johnson, D., and Spice, A.: The measurement and parameterization of effective radius of droplets in warm stratocumulus clouds, *J. Atmos. Sci.*, 51, 1823–1842, 1994. 21940
- Mayer, B. and Kylling, A.: Technical note: The libRadtran software package for radiative transfer calculations – description and examples of use, *Atmos. Chem. Phys.*, 5, 1855–1877, doi:10.5194/acp-5-1855-2005, 2005. 21941
- 5 Mayer, B., Seckmeyer, G., and Kylling, A.: Systematic long-term comparison of spectral UV measurements and UVSPEC modeling results, *J. Geophys. Res.*, 102, 8755–8767, 1997. 21941
- McFarquhar, G. and Heymsfield, A.: The definition and significance of an effective radius for ice clouds, *J. Atmos. Sci.*, 55, 2039–2052, 1998. 21959
- 10 McFarquhar, G., Iacobellis, S., and Somerville, R.: SCM simulations of tropical ice clouds using observationally based parameterizations of microphysics, *J. Climate*, 16, 1643–1664, 2003. 21940
- Meirink, J., Roebeling, R., Wolters, E., and Deneke, H.: Cloud Physical Products AVHRR / SEVIRI, Algorithm Theoretical Basis Document SAF/CM/KNMI/ATBD/CP 1.0, 12.2.2010, EUMETSAT SAF on Climate Monitoring, 2010. 21946
- 15 Menzel, W., Smith, W., and Stewart, T.: Improved cloud motion wind vector and altitude assignment using VAS, *J. Appl. Meteorol.*, 22, 377–384, 1983. 21945, 21948
- Menzel, W., Wylie, D., and Strabala, K.: Seasonal and diurnal changes in cirrus clouds as seen in four years of observations with the VAS, *J. Appl. Meteorol.*, 31, 370–385, 1992. 21955
- 20 Minnis, P., Liou, K.-N., and Takano, Y.: Inference of cirrus cloud properties using satellite-observed visible and infrared radiances. Part I: Parameterization of radiance fields, *J. Atmos. Sci.*, 50, 1279–1304, 1993. 21948
- Nakajima, T. and King, M. D.: Determination of the optical thickness and effective particle radius of clouds from reflected solar radiation measurements. Part I: theory, *J. Atmos. Sci.*, 47, 1878–1893, 1990. 21946, 21948
- 25 Nakajima, T. and Nakajima, T.: Wide-area determination of cloud microphysical properties from NOAA AVHRR measurements for FIRE and ASTEX regions, *J. Atmos. Sci.*, 52, 4043–4059, 1995. 21946, 21948
- 30 Nakajima, T. and Tanaka, M.: Effect of wind-generated waves on the transfer of solar radiation in the atmosphere-ocean system, *J. Quant. Spectrosc. Ra.*, 29, 521–537, 1983. 21942
- Nieman, S., Schmetz, J., and Menzel, W.: A comparison of several techniques to assign heights to cloud tracers, *J. Appl. Meteorol.*, 32, 1559–1568, 1993. 21945, 21948

- Pierluissi, J. and Peng, G.-S.: New molecular transmission band models for LOWTRAN, *Optical Engineering*, 24, 541–547, 1985. 21942
- Pinsky, M. and Khain, A.: Fine structure of cloud droplet concentration as seen from Fast-FSSP measurements. Part II: Results of in-situ observations, *J. Appl. Meteorol.*, 42, 65–73, 2003. 21938
- 5 Platnick, S.: Vertical photon transport in cloud remote sensing problems, *J. Geophys. Res.*, 105, 22919–22935, 2000. 21959, 21960
- Reuter, M., Thomas, W., Albert, P., Lockhoff, M., Weber, R., Karlsson, K.-G., and Fischer, J.: The CM-SAF and FUB Cloud Detection Schemes for SEVIRI: Validation with Synoptic Data and Initial Comparison with MODIS and CALIPSO, *J. Appl. Meteorol. Climatol.*, 48, 301–316, doi:10.1175/2008JAMC1982.1, 2009. 21952
- 10 Ricchiazzi, P., Yang, S., Gautier, C., and Soble, D.: SBDART: A research and Teaching software tool for plane-parallel radiative transfer in the Earth's atmosphere, *B. Am. Meteorol. Soc.*, 79, 2101–2114, 1998. 21942
- 15 Roebeling, R., Feijt, A., and Stammes, P.: Cloud property retrievals for climate monitoring: Implications of differences between Spinning Enhanced Visible and Infrared Imager (SEVIRI) on METEOSAT-8 and Advanced Very High Resolution Radiometer (AVHRR) on NOAA-17, *J. Geophys. Res.*, 111, D20210, doi:10.1029/2005JD006990, 2006. 21946, 21948, 21949
- Rossow, W. and Schiffer, R.: Advances in understanding clouds from ISCCP, *B. Am. Meteorol. Soc.*, 80, 2261–2287, 1999. 21949
- 20 SAFNWC: Product User Manual for Cloud Products (CMa-PGE01, CT-PGE02 & CTT-PGE03 v1.4), SAF/NWC/CDOP/MFL/SCI/PUM/01 Issue 1, Rev. 4, 7 November 2007, Météo-France, applicable to SAFNWC/MSG version 2008, 2007. 21946, 21947
- Saunders, R. and Kriebel, K.: An improved method for detecting clear sky and cloudy radiances from AVHRR data, *Int. J. Remote Sens.*, 9, 123–150, 1988. 21944
- 25 Saunders, R., English, S., Rayer, P., Matricardi, M., Chevallier, F., Brunel, P., and Deblonde, G.: RTTOV-7: A Satellite Radiance Simulator for the New Millennium, in: Tech. Proc. ITSC-XII Lorne, 27 February–5 March 2002, 2002. 21947
- 30 Schaaf, C., Gao, F., Strahler, A., Lucht, W., Li, X., Tsang, T., Strugnell, N., Zhang, X., Jin, Y., Muller, J.-P., Lewis, P., Barnsley, M., Hobson, P., Disney, M., Roberts, G., Dunderdale, M., Doll, C., d'Entremont, R., Hu, B., Liang, S., and Privette, J.: First Operational BRDF, Albedo and Nadir Reflectance Products from MODIS, *Remote Sens. Environ.*, 83, 135–148, 2002. 21942

Validation of retrievals with simulated dataL. Bugliaro et al.

[Title Page](#)[Abstract](#)[Introduction](#)[Conclusions](#)[References](#)[Tables](#)[Figures](#)[◀](#)[▶](#)[◀](#)[▶](#)[Back](#)[Close](#)[Full Screen / Esc](#)[Printer-friendly Version](#)[Interactive Discussion](#)

Validation of retrievals with simulated data

L. Bugliaro et al.

Title Page

Abstract

Introduction

Conclusions

References

Tables

Figures

◀

▶

◀

▶

Back

Close

Full Screen / Esc

Printer-friendly Version

Interactive Discussion



- Schmetz, J., Holmlund, K., Hoffman, J., Strauss, B., Mason, B., Gaertner, V., Koch, A., and van de Berg, L.: Operational cloud-motion winds from Meteosat infrared Images, *J. Appl. Meteorol.*, 32, 1206–1225, 1993. 21945
- Schmetz, J., Pili, P., Tjemkes, S., Just, D., Kerkmann, J., Rota, S., and Ratier, A.: An introduction to Meteosat Second Generation (MSG), *B. Am. Meteorol. Soc.*, 83, 977–992, 2002. 21971
- Schumann, U., Mayer, B., Gierens, K., Unterstrasser, S., Jessberger, P., Petzold, A., and Voigt, C.: Effective Radius of Ice Particles in Cirrus and Contrails, *J. Atmos. Sci.*, submitted, 2010. 21959
- Schutgens, N. and Roebeling, R.: Validating the Validation: The Influence of Liquid Water Distribution in Clouds on the Intercomparison of Satellite and Surface Observations, *J. Atmos. Ocean. Tech.*, 26, 1457–1474, 2009. 21950
- Shettle, E.: Models of aerosols, clouds and precipitation for atmospheric propagation studies, in: Atmospheric propagation in the uv, visible, ir and mm-region and related system aspects, no. 454 in AGARD Conference Proceedings, 1989. 21942
- Smith, W. and Platt, C.: Intercomparison of radiosonde, ground-based laser, and satellite-deduced cloud heights, *J. Appl. Meteorol.*, 17, 1796–1802, 1978. 21948
- Smith, W., Woolf, H., and Jacob, W.: A regression method for obtaining real-time temperature and geopotential height profiles from satellite spectrometer measurements and its application to Nimbus-3 SIRS observations, *Mon. Weather Rev.*, 98, 604–611, 1970. 21948
- Smith, W., Woolf, H., Abel, P., Hayden, C., Chalfant, M., and Grody, N.: Nimbus 5 sounder data processing system, 1, Measurement characteristics and data reduction procedures, NOAA Tech. Memo. NESS 57, Natl. Oceanic and Atmos. Admin., Silver Spring, Md., 1974. 21948
- Stammes, P.: Spectral radiance modelling in the UV-Visible range, in: IRS 2000: Current problems in atmospheric radiation, edited by Smith, W. and Timofeyev, Y., Proceedings of the International Radiation Symposium, A. Deepak Publishing, 385–388, 2001. 21949
- Stammes, P., Acarreta, J., Knap, W., and Tilstra, L.: Earth reflectance spectra from 300–1750 nm measured by SCIAMACHY, in: IRS 2004: Current problems in atmospheric radiation, edited by Fischer, H. and Sohn, B.-J., Proceedings of the International Radiation Symposium, A. Deepak Publishing, 2005. 21949
- Stamnes, K., Tsay, S., Wiscombe, W., and Jayaweera, K.: A numerically stable algorithm for discrete-ordinate-method radiative transfer in multiple scattering and emitting layered media, *Appl. Optics*, 27, 2502–2509, 1988. 21942

Validation of retrievals with simulated data

L. Bugliaro et al.

Title Page

Abstract

Introduction

Conclusions

References

Tables

Figures

◀

▶

◀

▶

Back

Close

Full Screen / Esc

Printer-friendly Version

Interactive Discussion



- Stamnes, K., Tsay, S.-C., Wiscombe, W., and Laszlo, I.: DISORT, a General-Purpose Fortran Program for Discrete-Ordinate-Method Radiative Transfer in Scattering and Emitting Layered Media: Documentation of Methodology, Tech. rep., Dept. of Physics and Engineering Physics, Stevens Institute of Technology, Hoboken, NJ 07030, 2000. 21942
- 5 Stephens, G.: Radiation profiles in extended water clouds. II: Parameterization schemes, *J. Atmos. Sci.*, 35, 2123–2132, 1978. 21949
- Stoppel, J., Doms, G., Schättler, U., Bitzer, H., Gassmann, A., Damrath, U., and Gregoric, G.: Meso-gamma scale forecasts using the nonhydrostatic model LM, *Meteor. Atmos. Phys.*, 82, 75–96, 1997. 21936
- 10 Szejwach, G.: Determination of semi-transparent cirrus cloud temperatures from infrared radiances: Application to Meteosat, *J. Appl. Meteorol.*, 21, 384–393, 1982. 21945
- Tartaglione, N.: Relationship between Precipitation Forecast Errors and Skill Scores of Dichotomous Forecasts, *Weather Forecast.*, 25, 355–365, doi:10.1175/2009WAF2222211.1, 2010. 21952
- 15 Tiedtke, M.: A comprehensive mass flux scheme for cumulus parameterisation in large scale models, *Monthly Weather Review*, 117, 1779–1800, 1989. 21937
- Van Weele, M., Martin, T., Blumthaler, M., Brogniez, C., den Outer, P., Engelsen, O., Lenoble, J., Pfister, G., Ruggaber, A., Walravens, B., Weihs, P., Dieter, H., Gardiner, B., Gillotay, D., Kylling, A., Mayer, B., Seckmeyer, G., and Wauben, W.: From model intercomparisons towards benchmark UV spectra for six real atmospheric cases, *J. Geophys. Res.*, 105, 4915–4925, 2000. 21941
- 20 Venema, V., Garcia, S. G., and Simmer, C.: A new algorithm for the downscaling of cloud fields, *Q. J. Roy. Meteorol. Soc.*, 136, 91–106, doi:10.1002/qj.535, 2010. 21937
- Wan, Z. and Li, Z.-L.: A physics-based algorithm for retrieving land-surface emissivity and temperature from EOS/MODIS data, *IEEE T. Geosci. Remote*, 35, 980–996, 1997. 21942
- 25 Wolters, E., Roebeling, R., and Feijt, A.: Evaluation of Cloud-Phase Retrieval Methods for SEVIRI on Meteosat-8 Using Ground-Based Lidar and Cloud Radar Data, *J. Appl. Meteorol. Climatol.*, 47, 1723–1738, doi:10.1175/2007JAMC1591.1, 2008. 21949
- Woodcock, F.: The Evaluation of Yes/No Forecasts for Scientific and Administrative Purposes, *Mon. Weather Rev.*, 104, 1209–1214, doi:10.1175/1520-0493(1976)104<1209:TEOYFF>2.0.CO;2, 1976. 21952
- 30 Wyser, K. and Ström, J.: A possible change in cloud radiative forcing due to aircraft exhaust, *Geophys. Res. Lett.*, 25, 1673–1676, 1998. 21940

Yang, P., Liou, K., Wyser, K., and Mitchell, D.: Parameterization of the scattering and absorption properties of individual ice crystals, *J. Geophys. Res.*, 105, 4699–4718, 2000. 21941, 21946, 21958

5 Zinner, T. and Mayer, B.: Remote sensing of stratocumulus clouds: Uncertainty and biases due to inhomogeneity, *J. Geophys. Res.*, 111, D14209, doi:10.1029/2005JD006955, 2006. 21934, 21950

Validation of retrievals with simulated data

L. Bugliaro et al.

Title Page

Abstract

Introduction

Conclusions

References

Tables

Figures

⏪

⏩

◀

▶

Back

Close

Full Screen / Esc

Printer-friendly Version

Interactive Discussion



Validation of retrievals with simulated data

L. Bugliaro et al.

Title Page

Abstract

Introduction

Conclusions

References

Tables

Figures

◀

▶

◀

▶

Back

Close

Full Screen / Esc

Printer-friendly Version

Interactive Discussion



Table 1. SEVIRI spectral channels characteristics (Schmetz et al., 2002).

Channel	λ_{central} μm	λ_{min} μm	λ_{max} μm	Spatial Resolution km
VIS006	0.635	0.56	0.71	3
VIS008	0.81	0.74	0.88	3
IR_016	1.64	1.50	1.78	3
IR_039	3.90	3.48	4.36	3
WV_062	6.25	5.35	7.15	3
WV_073	7.35	6.85	7.85	3
IR_087	8.70	8.30	9.10	3
IR_097	9.66	9.38	9.94	3
IR_108	10.80	9.80	11.80	3
IR_120	12.00	11.00	13.00	3
IR_134	13.40	12.40	14.40	3
HRV	Broadband (about 0.4–1.1)			1

Table 2. Summary of real cloud properties after projection to the MET-8/SEVIRI grid. CTP = Cloud Top Phase, WC = Water Cloud, IC = Ice Cloud, CC = Cloud Cover, CTT = Cloud Top Temperature, CWP = Cloud Water Path, τ = Optical Thickness, r_{eff} = Effective Radius, σ_{τ} = Standard Deviation of Optical Thickness inside every single pixel.

	Cloudy	Clear	Total
# pixels	156 135	98 049	254 184
	Water Clouds	Ice Clouds	Multi-phase Clouds
# pixels	17 352	109 857	28 926
with CTP = WC	17 352	0	600
with CTP = IC	0	109 857	28 326
with CC = 1	13 504	100 644	28 452
with $0 < \text{CC} < 1$	3848	9213	474
Property	Water Clouds	Ice Clouds	Multi-phase Clouds
Min CTT/K	268.0	210.0	210.0
Max CTT/K	294.0	272.0	279.0
Mean CTT/K	282.6	222.6	226.4
Std CTT/K	3.6	6.4	8.8
Min CWP/g m ⁻²	4.31e-4	2.75e-4	0.107
Max CWP/g m ⁻²	904.40	2239.7	6241.8
Mean CWP/g m ⁻²	35.37	69.19	187.42
Std CWP/g m ⁻²	37.44	112.82	323.20
Min τ	8.10e-4	5.47e-6	9.94e-3
Max τ	150.0	46.00	224.85
Mean τ	9.13	2.15	17.42
Std τ	7.45	2.71	22.46
Min $r_{\text{eff}}/\mu\text{m}$	1.0	10.97	1.0
Max $r_{\text{eff}}/\mu\text{m}$	11.79	84.22	84.22
Mean $r_{\text{eff}}/\mu\text{m}$	4.90	53.60	44.75
Min σ_{τ}	4.32e-4	9.06e-6	9.99e-05
Max σ_{τ}	43.54	7.07	72.05
Mean σ_{τ}	1.51	0.14	2.88
Std σ_{τ}	1.84	0.16	4.06

Validation of retrievals with simulated data

L. Bugliaro et al.

Title Page

Abstract

Introduction

Conclusions

References

Tables

Figures

◀

▶

◀

▶

Back

Close

Full Screen / Esc

Printer-friendly Version

Interactive Discussion



Validation of retrievals with simulated data

L. Bugliaro et al.

Title Page

Abstract

Introduction

Conclusions

References

Tables

Figures

⏪

⏩

◀

▶

Back

Close

Full Screen / Esc

Printer-friendly Version

Interactive Discussion



Table 3. Contingency table applied to every pixel of the simulated scene.

Scenario		Retrieval		Total
		Cloud free	Cloudy	
Reality	Cloud free	a	b	$a + b$
	Cloudy	c	d	$c + d$
	Total	$a + c$	$b + d$	$N = a + b + c + d$

Validation of retrievals with simulated data

L. Bugliaro et al.

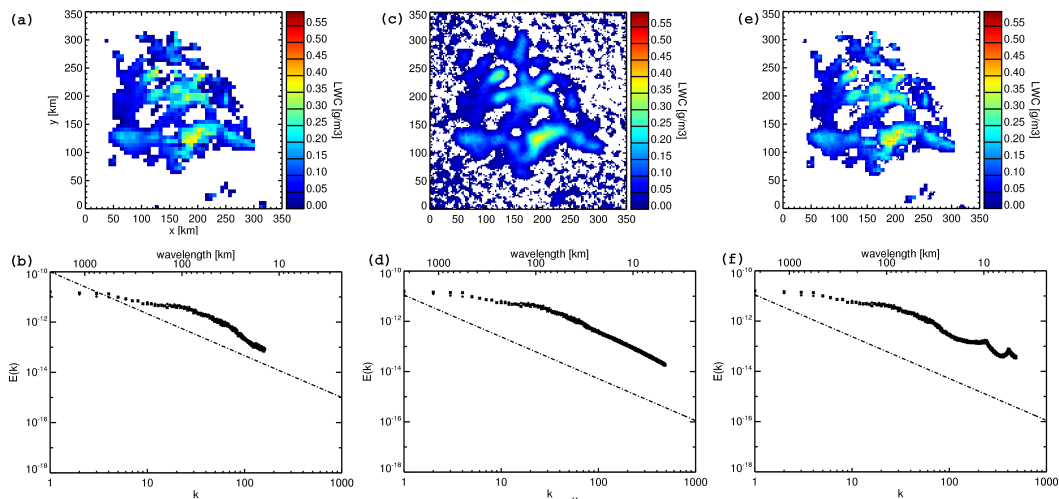


Fig. 1. Downscaling of a layer of LWC from the COSMO-EU model: Shown is the water content field from COSMO-EU (a) through the iteration steps (b) leading to the final downscaled field (c). Through the process negative LWC values are allowed (visible in the spurious positive water content throughout the cloud free areas in c). These values are set to zero in (e). (b), (d), and (f) show the related power spectra.

[Title Page](#)
[Abstract](#)
[Introduction](#)
[Conclusions](#)
[References](#)
[Tables](#)
[Figures](#)
[⏪](#)
[⏩](#)
[◀](#)
[▶](#)
[Back](#)
[Close](#)
[Full Screen / Esc](#)
[Printer-friendly Version](#)
[Interactive Discussion](#)

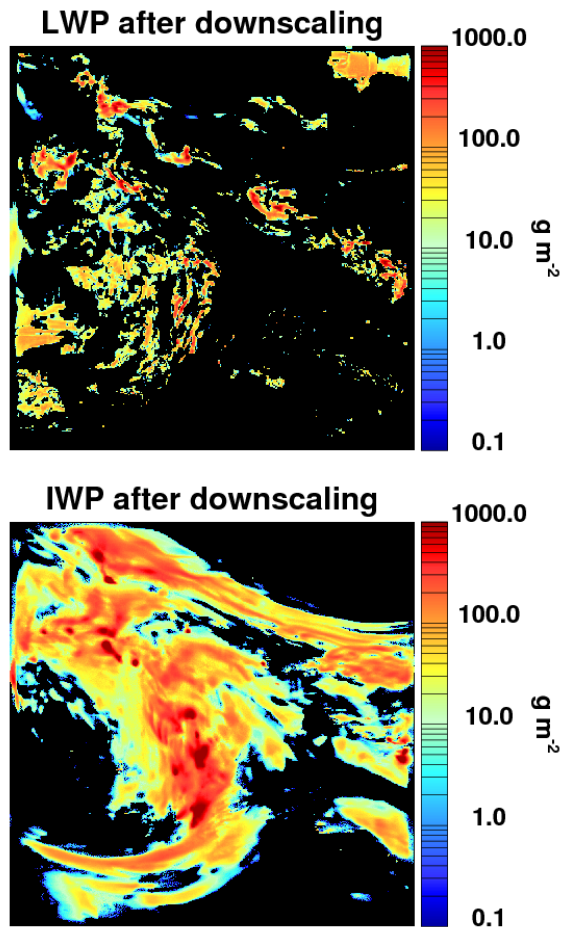



Fig. 2. Cloud liquid water (top) and cloud ice (bottom) for the COSMO-EU grid after resolution enhancement.

Validation of retrievals with simulated data

L. Bugliaro et al.

Title Page

Abstract Introduction

Conclusions References

Tables Figures

◀ ▶

◀ ▶

Back Close

Full Screen / Esc

Printer-friendly Version

Interactive Discussion



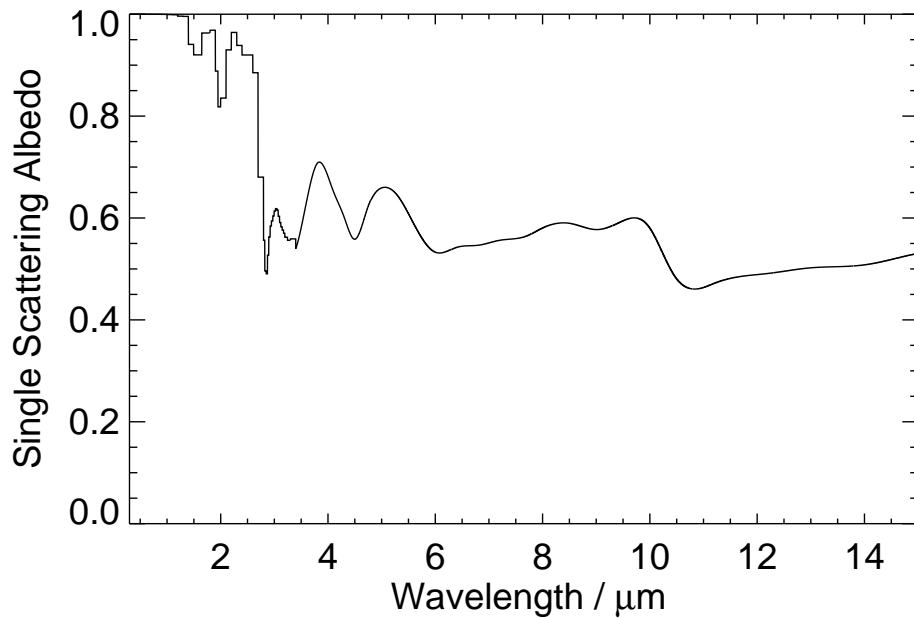


Fig. 3. Single scattering albedo for hexagonal ice crystals of $30\ \mu\text{m}$ effective radius for the ice cloud parameterisation used.

Validation of retrievals with simulated data

L. Bugliaro et al.

Title Page

Abstract Introduction

Conclusions References

Tables Figures

◀ ▶

◀ ▶

Back Close

Full Screen / Esc

Printer-friendly Version

Interactive Discussion



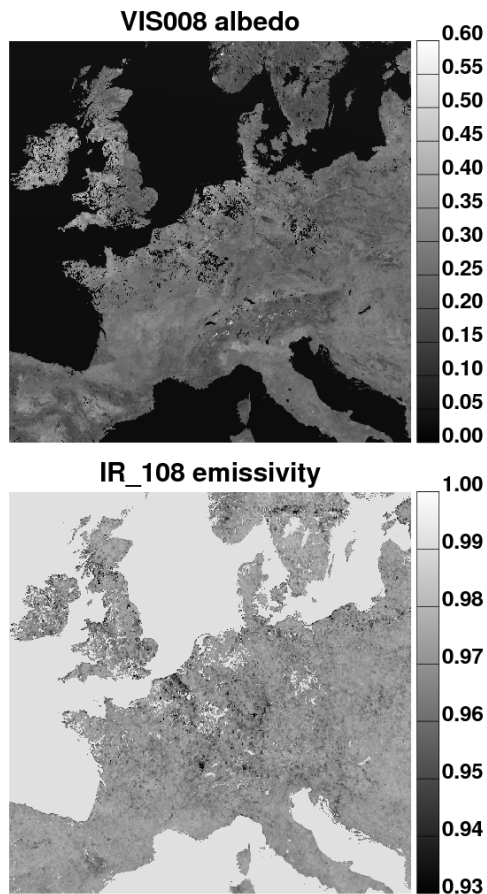


Fig. 4. Example of (top) SEVIRI albedo for channel VIS008 and (bottom) SEVIRI emissivity for channel IR_108. Both quantities have been extracted from MODIS products and are displayed on the resolution enhanced COSMO-EU grid.

Validation of retrievals with simulated data

L. Bugliaro et al.

Title Page

Abstract Introduction

Conclusions References

Tables Figures

◀ ▶

◀ ▶

Back Close

Full Screen / Esc

Printer-friendly Version

Interactive Discussion



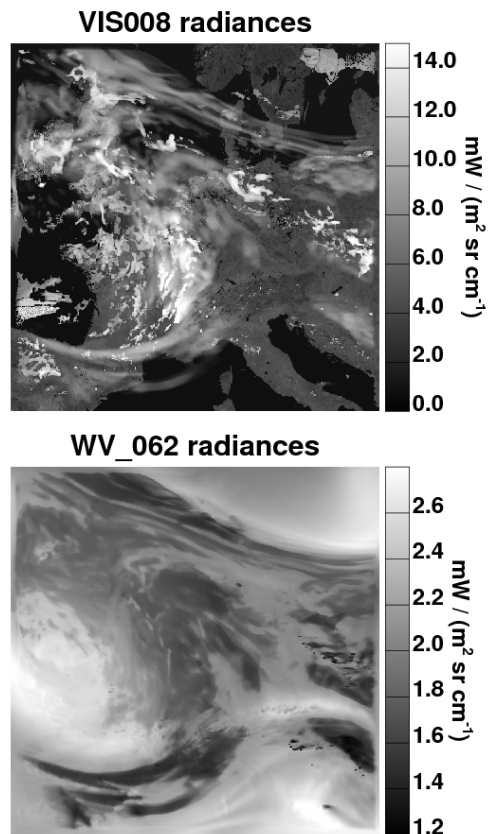


Fig. 5. Example of SEVIRI radiances computed with libRadtran: (top) solar channel VIS008 centred at $0.8\ \mu\text{m}$ and (bottom) water vapour channel WV_062 centred at $6.2\ \mu\text{m}$. Both plots are on the MODEL grid.

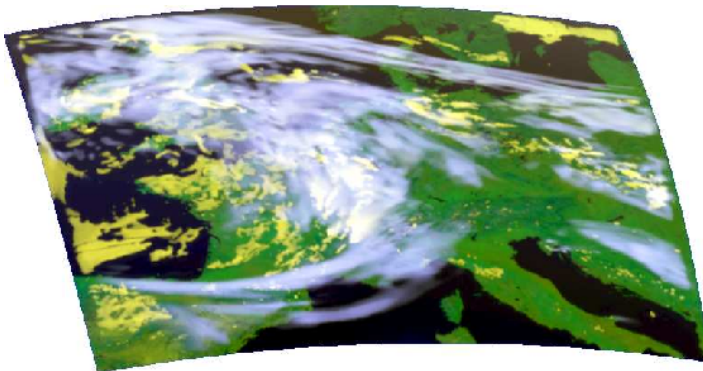


Fig. 6. (Top) false color composites of a real MET-8/SEVIRI observation from 12 August 2004, 12:00 UTC; (bottom) simulated satellite observation, for the same date and time and processed by the same false color algorithm.

Validation of retrievals with simulated data

L. Bugliaro et al.

Title Page

Abstract

Introduction

Conclusions

References

Tables

Figures

◀

▶

◀

▶

Back

Close

Full Screen / Esc

Printer-friendly Version

Interactive Discussion



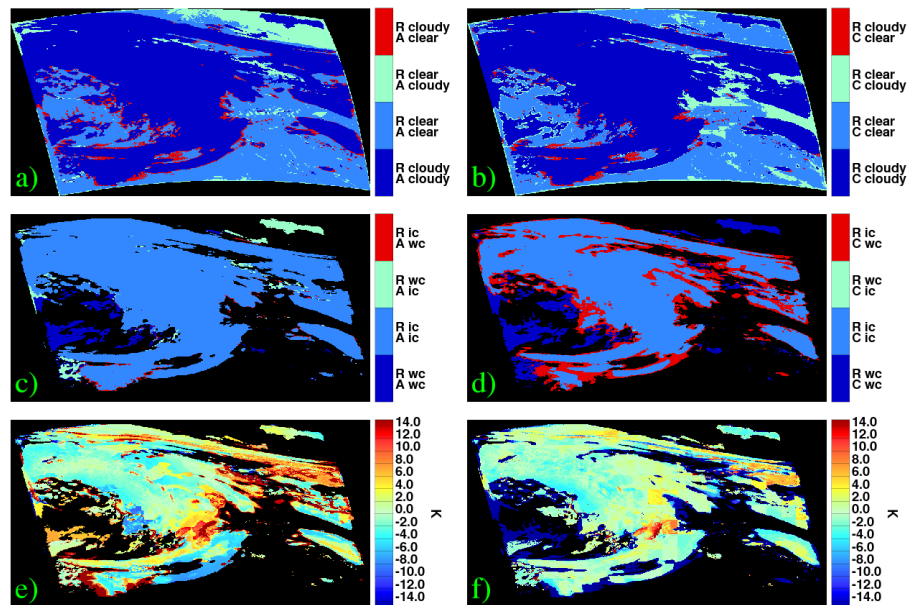


Fig. 7. Differences between retrieval results and real cloud properties. **(a)** Differences between real and APICS cloud mask. “R clear/cloudy” means that the pixel is really clear/cloudy, “A clear/cloudy” means that the pixel is cloudy/clear according to the APICS retrieval. **(b)** Differences between real and CMSAF cloud mask. “R clear/cloudy” means that the pixel is really clear/cloudy, “C clear/cloudy” means that the pixel is cloudy/clear according to the CMSAF retrieval. **(c)** Differences between real and APICS cloud top phase. “R wc/ic” means that the pixel contains a real water/ice cloud, “A wc/ic” means that the pixel contains a water/ice cloud according to APICS. **(d)** Differences between real and CMSAF cloud top phase. “R wc/ic” means that the pixel contains a real water/ice cloud, “C wc/ic” means that the pixel contains a water/ice cloud according to CMSAF. **(e)** Difference between retrieved and real cloud top temperatures for APICS. **(f)** Difference between retrieved and real cloud top temperatures for CMSAF.

Validation of retrievals with simulated data

L. Bugliaro et al.

Title Page

Abstract Introduction

Conclusions References

Tables Figures

◀ ▶

◀ ▶

Back Close

Full Screen / Esc

Printer-friendly Version

Interactive Discussion



Validation of retrievals with simulated data

L. Bugliaro et al.

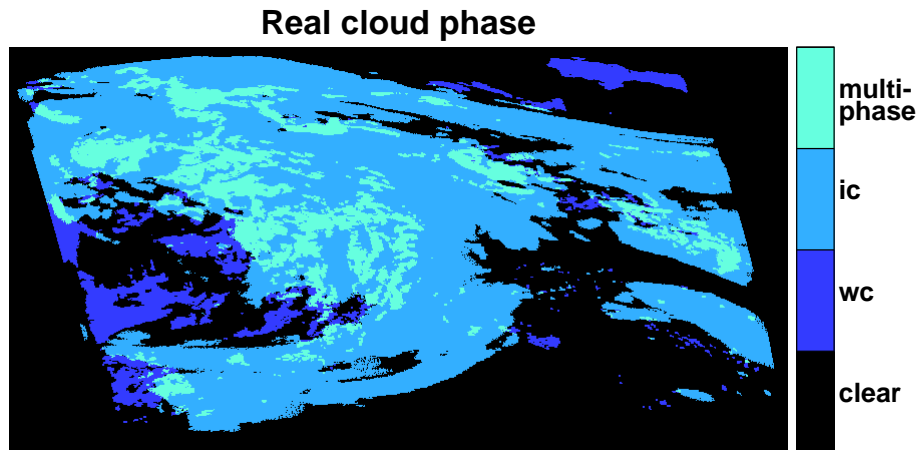


Fig. 8. Real cloud phase on the MET-8/SEVIRI grid: water clouds and ice clouds denote pixels containing exclusively liquid or iced cloud constituents. For an explanation of multi-phase clouds see the text.

[Title Page](#)[Abstract](#)[Introduction](#)[Conclusions](#)[References](#)[Tables](#)[Figures](#)[I◀](#)[▶I](#)[◀](#)[▶](#)[Back](#)[Close](#)[Full Screen / Esc](#)[Printer-friendly Version](#)[Interactive Discussion](#)

Validation of retrievals with simulated data

L. Bugliaro et al.

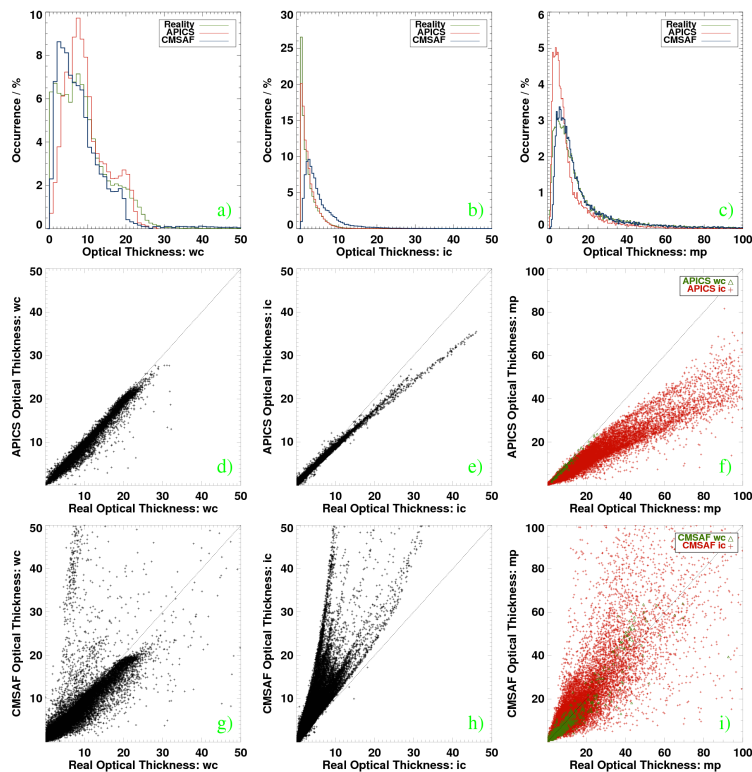


Fig. 9. Histograms and scatter plots of retrieved and real cloud optical thickness for both APICS and CMSAF. **(a–c)** histograms of retrieved and real optical thickness of water, ice and multi-phase clouds for both APICS and CMSAF. **(d–f)** Scatter plots of APICS optical thicknesses against real optical thicknesses for water, ice and multi-phase clouds. **(g–i)** Scatter plots of CMSAF optical thicknesses against real optical thicknesses for water, ice and multi-phase clouds.

Title Page

Abstract

Introduction

Conclusions

References

Tables

Figures

◀

▶

◀

▶

Back

Close

Full Screen / Esc

Printer-friendly Version

Interactive Discussion

Validation of retrievals with simulated data

L. Bugliaro et al.

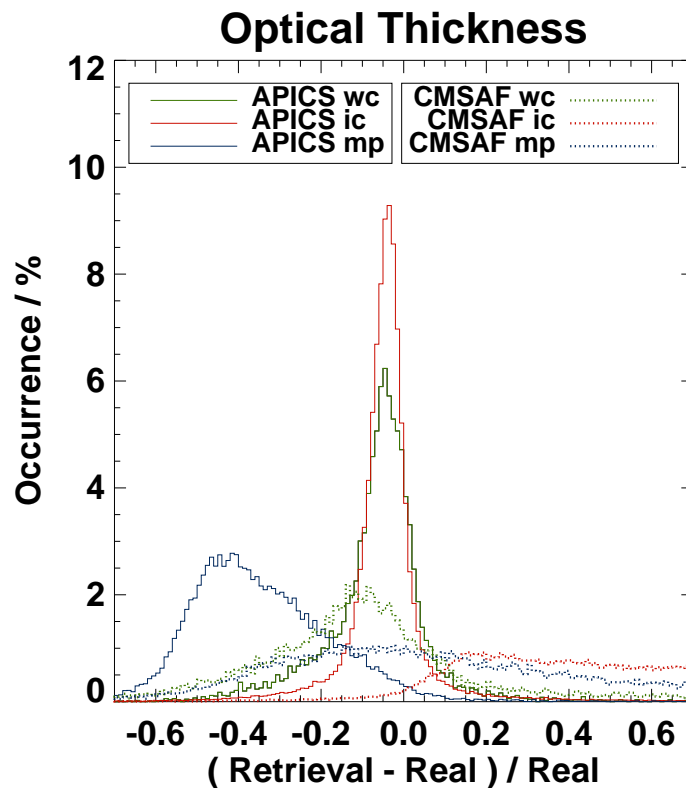


Fig. 10. Histograms of relative differences between retrieved and real cloud optical thickness for water (green), ice (red) and multi-phase (blue) clouds. Solid lines denote APICS retrieval results, dotted lines CMSAF retrieval results.

[Title Page](#)[Abstract](#)[Introduction](#)[Conclusions](#)[References](#)[Tables](#)[Figures](#)[◀](#)[▶](#)[◀](#)[▶](#)[Back](#)[Close](#)[Full Screen / Esc](#)[Printer-friendly Version](#)[Interactive Discussion](#)

Validation of retrievals with simulated data

L. Bugliaro et al.

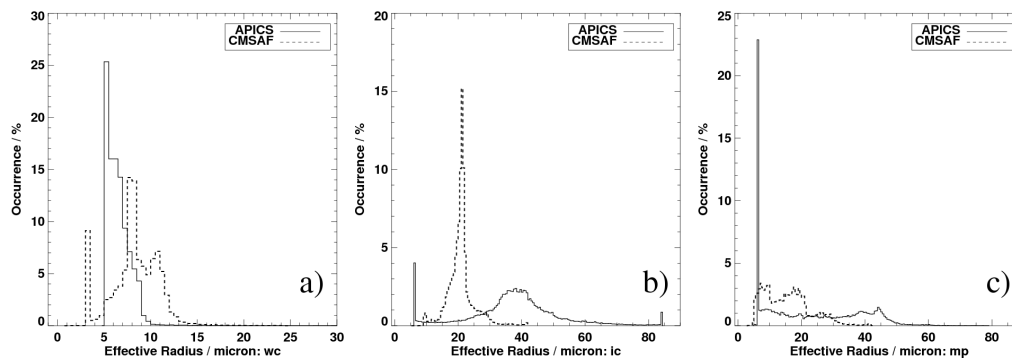


Fig. 11. Histograms of effective radius occurrence for APICS and CMSAF for **a)** water clouds (wc), **b)** ice clouds (ic) and **c)** multi-phase clouds (mp).

Title Page

Abstract

Introduction

Conclusions

References

Tables

Figures

◀

▶

◀

▶

Back

Close

Full Screen / Esc

Printer-friendly Version

Interactive Discussion



Validation of retrievals with simulated data

L. Bugliaro et al.

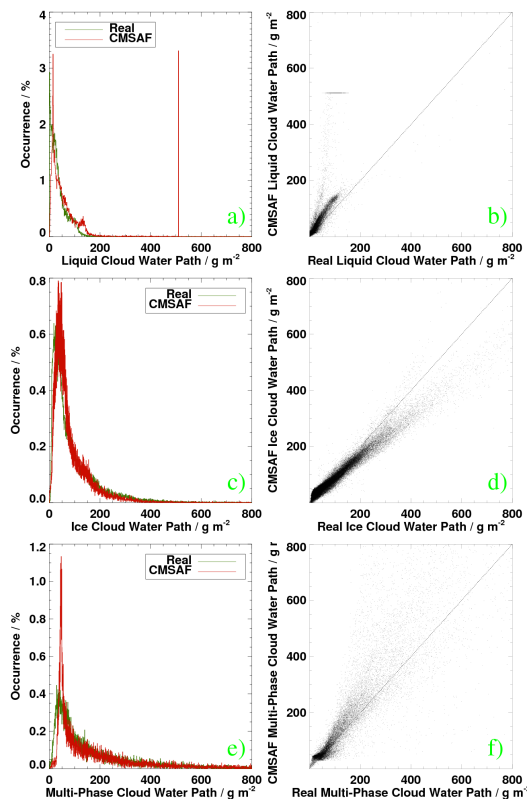


Fig. 12. CMSAF evaluation of cloud water path. **(a)** Histograms of retrieved and real cloud liquid water path. **(b)** Scatter plots of retrieved versus real liquid cloud water path. **(c)** Histograms of retrieved and real cloud ice water path. **(d)** Scatter plots of retrieved versus real ice cloud water path. **(e)** Histograms of retrieved and real cloud water path for multi-phase clouds. **(f)** Scatter plots of retrieved versus real cloud water path for multi-phase clouds.

[Title Page](#)
[Abstract](#)
[Introduction](#)
[Conclusions](#)
[References](#)
[Tables](#)
[Figures](#)
[◀](#)
[▶](#)
[◀](#)
[▶](#)
[Back](#)
[Close](#)
[Full Screen / Esc](#)
[Printer-friendly Version](#)
[Interactive Discussion](#)


Validation of retrievals with simulated data

L. Bugliaro et al.

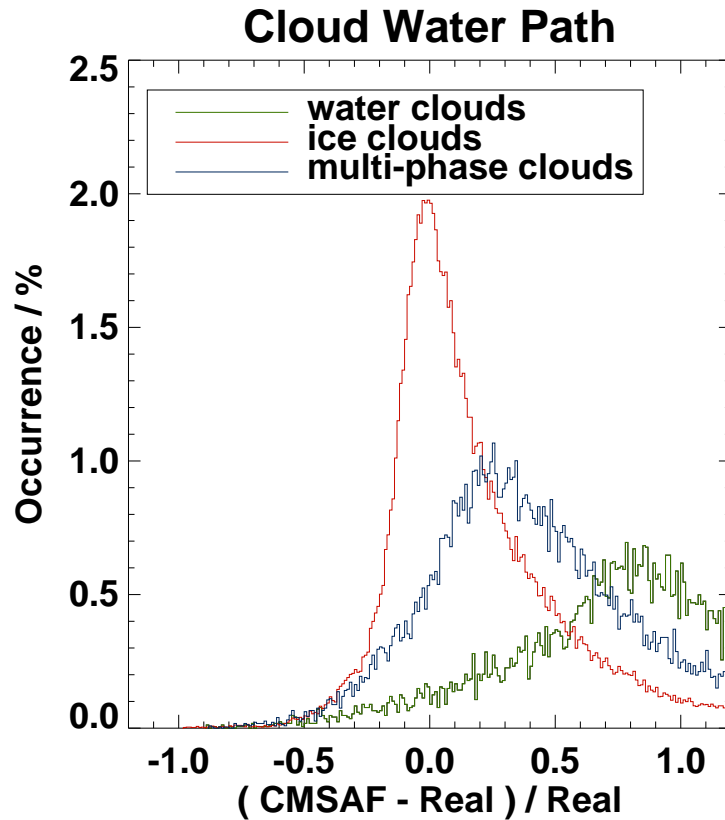


Fig. 13. Histograms of relative differences between CMSAF and real cloud water paths for water (green), ice (red) and multi-phase (blue) clouds.

[Title Page](#)[Abstract](#)[Introduction](#)[Conclusions](#)[References](#)[Tables](#)[Figures](#)[◀](#)[▶](#)[◀](#)[▶](#)[Back](#)[Close](#)[Full Screen / Esc](#)[Printer-friendly Version](#)[Interactive Discussion](#)

Appendix A Simulation Results

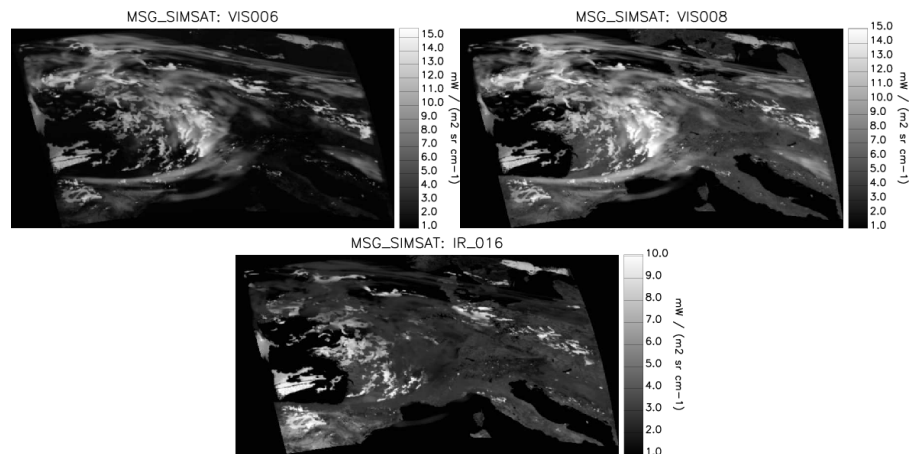


Fig. A1. Solar SEVIRI radiances computed with libRadtran and projected onto the nominal MET-8/SEVIRI grid under consideration of the MET-8/SEVIRI point spread functions.

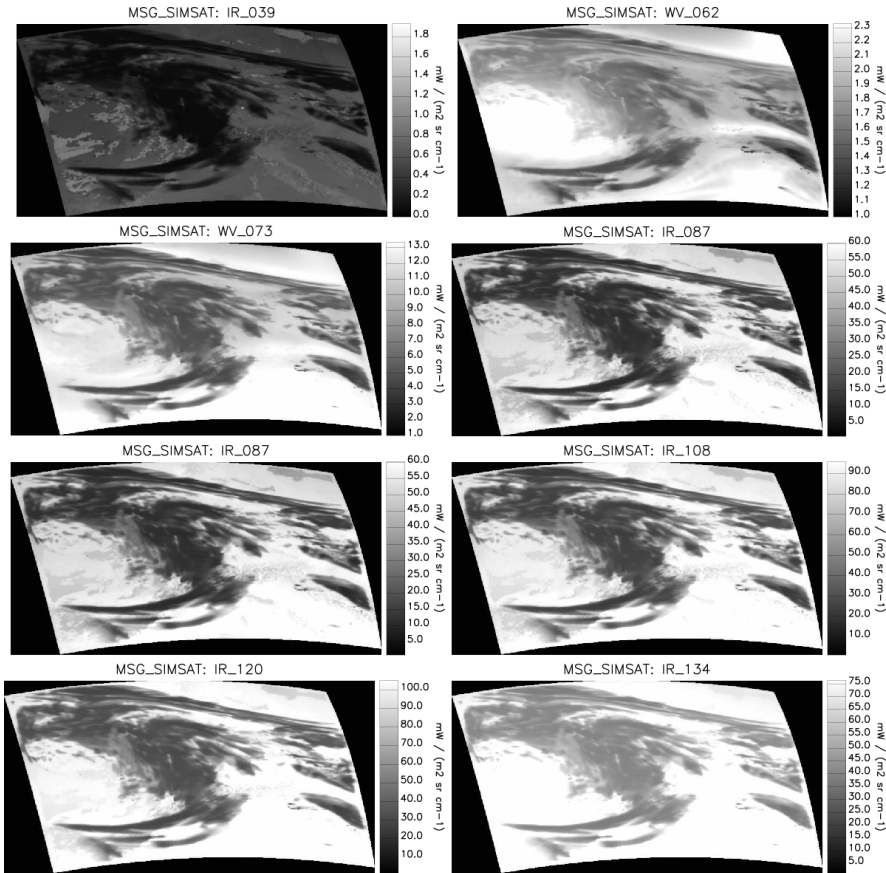


Fig. A2. Thermal SEVIRI radiances computed with libRadtran and projected onto the nominal MET-8/SEVIRI grid under consideration of the MET-8/SEVIRI point spread functions.

Validation of retrievals with simulated data

L. Bugliaro et al.

Title Page

Abstract Introduction

Conclusions References

Tables Figures

◀ ▶

◀ ▶

Back Close

Full Screen / Esc

Printer-friendly Version

Interactive Discussion

